Local Invariance Model for Short-Range Order in Binary Thermoelectrics

Litong Wu

St. Catherine's College

University of Oxford

Honour School of Chemistry: Chemistry Part II

Trinity 2023

Acknowledgements

I would like to express my sincere gratitude to Professor Andrew Goodwin, whose insightful comments greatly improved the quality of my work, and made me see the breadth and depth of science. It is an absolute honour to be supervised by Andrew; he will always be a role model in my future research career. I am deeply grateful to Nikolaj Roth, who guided me with patience and wisdom from the very beginning of this project. He shared with me not only the knowledge but also a scientific mindset to understand everything from its most fundamental principles. I am also appreciative of the support from all members of the Goodwin group throughout this year, especially Tom for his help with the DFT calculation.

Thank you to my most cherished friends, Muxue Chen, Xinyao Ma, and Yue Sun. Their support and company gave me strength during the worst time of my life. I wish them nothing but success as they truly deserve the best. A special thanks to Chenjing Bu, whose wisdom beyond our years and absolute passion for knowledge served as a guiding light for my thesis-writing journey. I have learnt so much from him in countless ways. Lastly, I am eternally grateful to my parents for the precious opportunity they have given me to study here, and everything else indeed. They are certainly the most supportive parents I could have ever wished for.

Abstract

Single-crystal diffuse scattering is an important feature found in the diffraction patterns of all crystalline materials, containing information about local structural correlations that cause deviations from perfect periodicity. This feature, though crucial for relating structure to function, has been challenging to analyse due to the diversity and complexity of natural disorder effects. The aim of this thesis is to devise a generic modelling strategy for binary systems with occupational disorder. This method involves using a local invariance energy expression for Monte Carlo simulations of the disordered configurations.

This developed algorithm was applied to investigate the structural complexity of a potential thermoelectric material, $V_{1+\delta}Sb$. Single-crystal X-ray diffraction measurements and average structure refinement revealed substantial correlated disorder within the material. The 3D-ΔPDF analysis indicated the presence of occupational disorder of the excess vanadium atoms and the coupled displacive disorder of other atoms. Subsequent modelling generated atomistic configurations which produced diffraction patterns closely aligning with the experimental results. Potential modes of the disorder were concluded based on the model. The resulting features make $V_{1+\delta}Sb$ a promising candidate for potential thermoelectric application.

Contents

List of Figures

Abbreviations

3D-ΔPDF	3D difference pair distribution function
DFT	density functional theory
DoF	degree of freedom
DP	diffraction pattern
DS	diffuse scattering
FCC	face-centred cubic
FT	Fourier transform
HCP	hexagonal close-packed
LRO	long-range order
MC	Monte Carlo
RMC	reverse Monte Carlo
SC-XRD	single-crystal X-ray diffraction
SRO	short-range order
TE	thermoelectric

1

Introduction

Rising energy costs and escalating environmental pollution are pressing challenges that provoke scientists to look for efficient renewable energy sources and energy-harvesting technologies. Among these, thermoelectric (TE) materials stand out, exhibiting the ability to convert thermal energy directly into electricity through the Seebeck effect [1]. The tradeoff impeding the efficiency of TE materials is the paradoxical demand for high electric conductivity and minimal thermal conductivity [2]. One novel approach to circumvent this problem is through exploiting the intrinsic disorder present in complex crystal structures [3]. In this chapter, the concept of correlated disorder and its prospect to enhance TE performance of solid materials are explained, followed by an introduction of the standard methods employed to study correlated disordered structures.

1.1 Correlated disorder

A *crystal*, as defined by the International Union of Crystallography (IUCr) in the *Report of the Executive Committee for 1991*, is a solid in which its atoms, ions, or molecules form, on average, a *long-range ordered* arrangement [4]. Achieving this long-range order (LRO) typically requires a systematic and symmetrical assembly of specific building blocks. The structure of a crystal is then conventionally described by three basis vectors representing its 3D translational symmetry, and the coordinates of atoms within a unit cell.

However, from the absence of a common unit cell in incommensurate composite crystals, to the presence of crystallographically ‘forbidden’ symmetries in quasicrystals, it is clear that translational symmetry is not a definitive prerequisite for crystallinity [5]. Many crystals exhibit short-range order (SRO), wherein their overall structures cannot be described by translating any smaller part of them. Even though no clear repeating pattern can be seen at the local level, a semblance of average order persists on a larger scale. Importantly, this deviation from perfect periodicity is rarely random. Instead, it is mostly governed by the chemical, physical, and geometric properties of the constituent atoms. The presence of a particular atom type can influence the occupancy or displacement of another, giving rise to a phenomenon known as *correlated disorder* [6].

One cause of ground-state correlated disorder is an incompatibility between the local interactions and the lattice geometry. This is famously exemplified by the Ising model of anti-ferromagnetism on a triangular lattice [7]. In this model, the interaction between adjacent particles of opposite spins is favoured. Thus, simultaneous energy minimisation is impossible since each pair of opposing neighbours shares a common third neighbour. This type of frustration manifests in real-world spin structures such as Co-doped β-Mn [8] and $Ba_3CuSb_2O_9$ [9].

A second cause of correlated disorder, which holds greater relevance to the context of TE materials, is configurational flexibility. This occurs in cases where the atomic arrangement allows for multiple, energetically equivalent ways for the system to reach its ground state [6]. One common instance where this flexibility is observed is in pyrochlore lattices, exemplified by materials like $Y_2Mo_2O_7$ [10]. The pyrochlore structure, characterised by vertex-sharing tetrahedra, possesses some degrees of rotational and positional freedom for these tetrahedra that do not significantly alter the overall energy.

Regardless of the origin of the disorder, solid materials with correlated disorder exhibit useful physical properties which have been effectively harnessed in functional material design. For example, both high-temperature ceramics such as cubic zirconias [11] and high-T_c oxide superconductors such as $La_{2-x}Sr_xCuO_4$ [12], have disordered oxygen/vacancy arrays crucial for their respective properties. Furthermore, the disruption of translational periodicity is highly favourable for designing efficient thermoelectrics [13].

1.2 Link to thermoelectrics

Compared to other renewable energy sources such as solar, wind, and geothermal, which frequently come with high setup costs, waste heat remains a ubiquitous yet largely untapped energy source [14]. Thermoelectrics, which convert waste heat directly into useful electric energy, have yet to realise their potential due to the sub-optimal performance of TE materials. In these materials, the diffusion of mobile charge carriers down the temperature gradient leads to charge accumulation, producing a potential difference that can be used to power external loads [3].

The efficiency of this Seebeck effect is primarily characterised by the figure of merit (zT), given by

$$zT = \frac{S^2 \sigma T}{\kappa}, \tag{1}$$

which depends on the Seebeck coefficient (S), the electric conductivity (σ), the absolute temperature (T), and the thermal conductivity (κ). High-performance TE materials are generally characterised by a zT value greater than 1, while the exact benchmark may vary depending on the specific application and operating temperature range of the device [15].

A noticeable conflict in optimising TE efficiency arises from the contradictory requirements for high electrical conductivity, which necessitates unobstructed electron flow and crystallinity, and low thermal conductivity, which is commonly associated with amorphous materials. To reconcile this, the 'phonon-glass electron-crystal (PGEC)' concept has been introduced. This principle aims to design materials with reduced lattice thermal conductivity through phonon scattering, while preserving high electron mean free paths [16]. Notable examples of this design include the insertion of 'rattler' atoms in the large void of skutterudites such as $CoSb_3$ [17], and the half-Heusler alloys, which are made up of three interpenetrating face-centred cubic (FCC) sublattices, and work by having separate electron-crystal and phonon-glass substructures [18].

Sb-containing materials have gained significant interest for their use in TE applications, owing to their narrow bandgaps, complex structures caused by covalent bonding, and versatility to accommodate a wide variety of elements for doping or substitution. For instance, the alloy of Bi_2Te_3 and Sb_2Te_3 is one of the best near-room-temperature TE materials [19]. Other high-performance examples include the p-type Te/Ag/Ge/Sb (TAGS) alloys and bulk Zintl-phase materials, such as $Yb_{14}MnSb_{11}$ [3].

Recently, Zhang *et al.* reported a Zintl-phase TE material, Eu_2ZnSb_2 ($P6_3/mmc$), which demonstrated ultralow thermal conductivity and a maximum zT value close to 1 at 823 K upon increasing Zn deficiency. A comparison of its temperature-dependent zT values

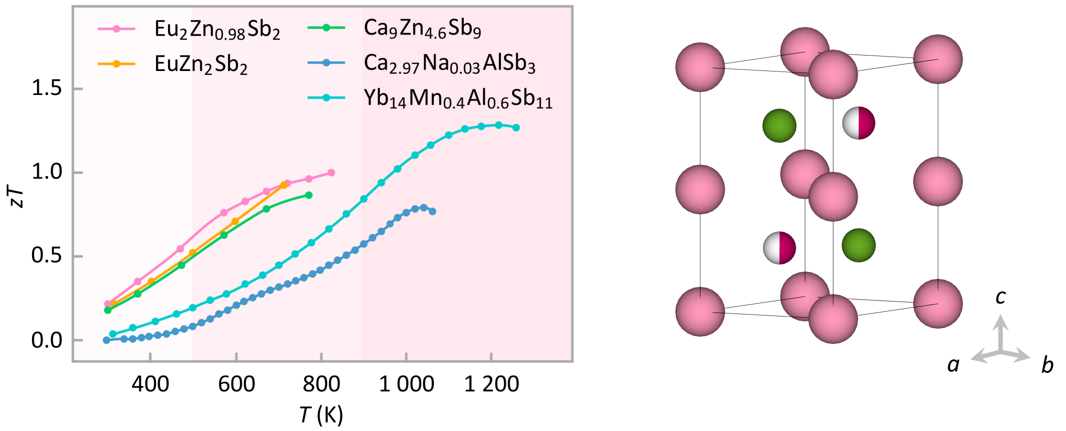

(a) (b)

Figure 1.1. **(a)** Plot of temperature-dependent *zT* values of some state-of-the-art p-type Zintl-phase TE materials, adapted from [20]. **(b)** Average unit cell of Eu_2ZnSb_2, with Eu in light pink, Zn in dark pink, and Sb in green.

with several leading-edge p-type Zintl-phase TE materials is presented in Figure 1.1 (a). The occupational disorder of Zn in the crystal structure of Eu_2ZnSb_2, as reflected by a partial occupancy in Figure 1.1 (b), is likely a key contributor to the effective phonon scattering in this material [20]. The material to be examined in Chapter 4, namely $V_{1+\delta}Sb$, shares the same space group and occupational disorder as Eu_2ZnSb_2. Indeed, $V_{1+\delta}Sb$ has garnered interest as a prospective candidate for TE applications. Our objective is to obtain a more comprehensive understanding of its potential by delving into the local details of its correlated disorder.

1.3 Diffuse scattering

Correlated disordered solids are typically studied by analysing diffraction patterns (DPs) obtained from single-crystal X-rays, neutrons, or electrons scattering experiments [6]. Most correlated disordered solids, despite their apparent lack of LRO, have average structures that can be described by one of the conventional crystallographic space groups. For example, Zn atoms are not consistently present at their expected locations in Eu_2ZnSb_2 —

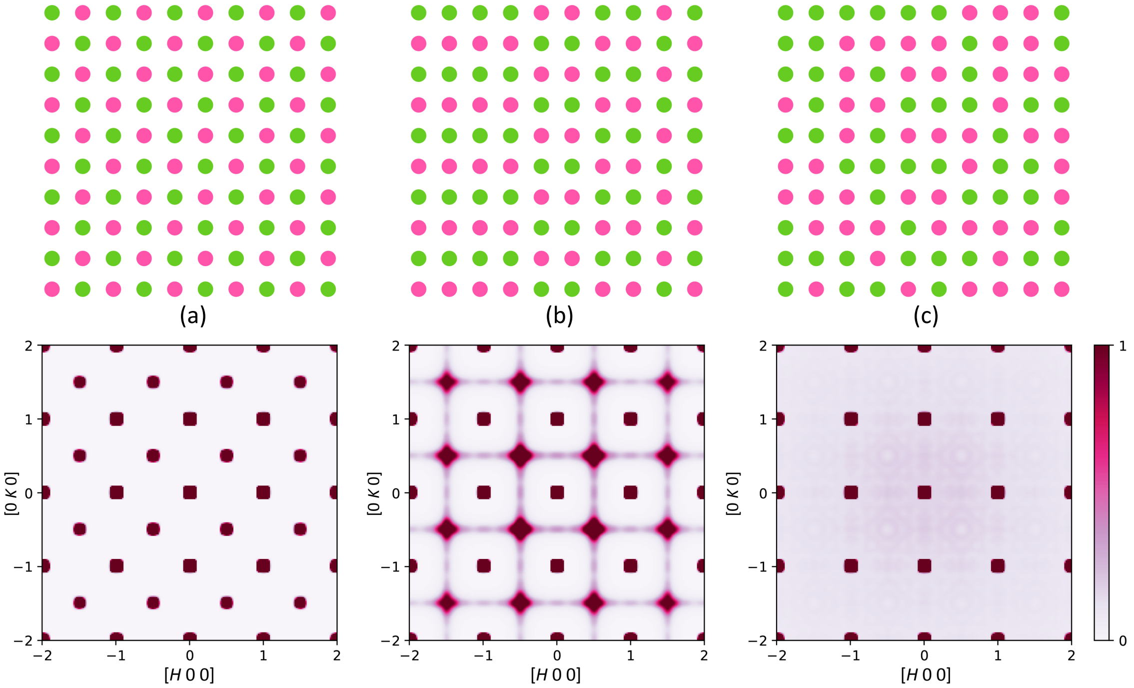

(d) (e) (f)

Figure 1.2. (a)–**(c)** Representative simulated configurations of a 2D binary system, with complete order, correlated disorder based on the local invariance rule, and random disorder. **(d)**–**(f)** Corresponding X-ray DPs, each computed from 20 configurations.

this is translated as a partial occupancy in the average structure shown in Figure 1.1 (b).

The Bragg peaks, which are the regularly spaced intense spots observed in single-crystal DPs, are routinely used to deduce the average arrangements of atoms. However, information regarding deviations away from this average, extending beyond the dimension of the unit cell, can only be extracted from the structured diffuse scattering (DS) — the weak, continuous scattering that occurs between the Bragg peaks [21].

To illustrate the concept of DS, a simple simulation of a 2D square lattice comprising two equal-proportion elements was performed and shown in Figure 1.2. Each column represents a different ordering rule, with example configurations displayed at the top, and corresponding DPs displayed at the bottom.

In the right column, a completely random distribution of particles on the square lattice produces a broad isotropic diffuse intensity centred at the origin. The Bragg peaks are generated from an average unit cell, with every lattice point occupied by the average electron density of the two elements. Conversely, the left column is derived from a completely ordered chequerboard arrangement of particles. In this case, DS is absent due to the perfect LRO. This also leads to a reduction in symmetry and a new unit cell twice the original size translating along the diagonal, resulting in additional Bragg peaks at half-integer values of H and K.

The lattice configuration in Figure 1.2 (b) was generated using a Monte Carlo (MC) simulation with the local invariance model (*c.f.* Section 2.4). Here, energy is optimised when all smallest four-atom squares within the structure contain two of each element, leading to configurational flexibility. This correlated disorder induces preferential distances between pairs of atoms, such that atoms of the same species often, but not always, position themselves two atoms apart. This is transformed into structured DS lines between the Bragg peaks in the DP as seen in Figure 1.2 (e).

Diffuse features have indeed been observed in numerous TE materials. Figure 1.3 (a) and (e) are the electron DPs of $Ag_{0.95}Pb_{15}SbTe_{17}$, a member of Pb/Sb/Ag/Te (LAST-m) TE family. The diffuse streaks indicate that the Ag, Sb, and Pb atoms tend to but are unable to attain an ordered arrangement [22]. Diffuse bands were also observed in the electron DPs of a series of defective 19-electron half-Heusler compounds. (b)–(d) show the changes in DS at different occupancy levels of Nb_xCoSb in the same plane; (f)–(h), of $Nb_{0.8}CoSb$ across different planes. The diffuse features suggest the existence of occupational disorder of the Nb/vacancy sublattice [23].

The analysis of the DS can provide valuable insights into the interplay of order and disor-

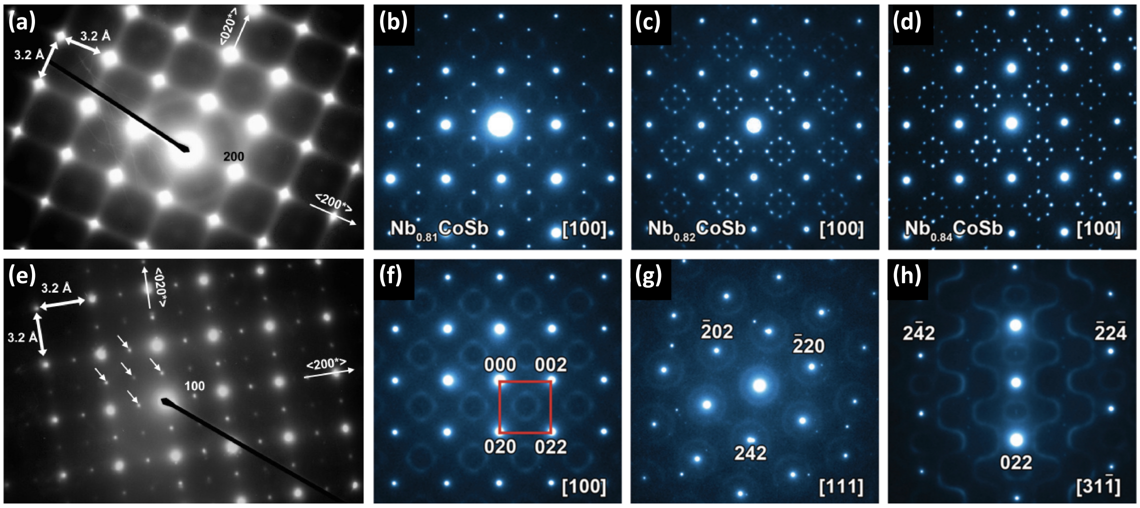

Figure 1.3. (**a**) and (**e**) Electron DPs of $Ag_{0.95}Pb_{15}SbTe_{17}$ with diffuse streaks and spots on [0 0 1] zone axis, sourced from [22]. (**b**)–(**d**) Electron DPs of $Nb_{0.81}CoSb$, $Nb_{0.82}CoSb$ and $Nb_{0.84}CoSb$ in the [1 0 0] direction. (**f**)–(**h**) Electron DPs of $Nb_{0.8}CoSb$ in the [1 0 0], [1 1 1] and [3 1 1] directions, sourced from [23].

der which often characterises efficient TE materials. Potentially, it can suggest possible strategies for adjusting the degree of order to allow property optimisation. However, the challenges in DS analysis primarily stem from two aspects: the measurement of DS and the subsequent modelling of the disorder [24].

1.3.1 Measurement of diffuse scattering

DS are typically obtained from single-crystal diffraction measurements. This thesis focuses on single-crystal X-ray diffraction (SC-XRD) due to its relevance to the measurements taken in Chapter 4. During the measurement, a large and high-quality crystal is mounted onto a polymer loop. The mounted crystal is then placed on a goniometer and aligned with the rotation centre of the diffractometer for subsequent measurement.

The difficulties associated with DS measurements primarily stem from two factors. First, diffuse intensities are usually 3–4 orders of magnitude weaker than typical Bragg intensities. Second, it is necessary to measure the scattering as far as possible in 3D, as DS is found throughout the reciprocal space and can be anisotropic [25]. These factors impose stringent requirements on both crystals and instruments.

In terms of the X-ray sources, the use of high-energy and high-intensity monochromatic X-rays is essential for retrieving short-range information at precise positions, while maintaining a satisfactory signal-to-noise ratio. Within the laboratory, X-rays are typically produced from the Kα electronic de-excitation when accelerated electrons strike a metal (usually Mo or Cu). For more precise measurements, synchrotron radiation, which is emitted when an electron beam is accelerated by electromagnetic fields, can be employed. Synchrotron sources are capable of generating highly collimated and wavelength-tunable radiation, offering greater control in X-ray experiments [26].

Regarding detector systems, single-photon counting pixel detectors are among the most advanced ones, capable of offering a high signal-to-noise ratio, good resolution, and a broad dynamic range [27]. A complete set of high-resolution DS is then collected by rotating the crystal and measuring the scattered X-rays at different detector angles. Capturing these weak diffuse features also necessitates a long exposure time. A cryostream is employed to regulate the experimental temperature [28].

Thanks to the advancements in X-ray sources and the increasing accessibility of large-area detectors, the acquisition of high-quality DS data has become substantially more manageable, as long as large and high-quality crystals are available.

1.3.2 Analysis of diffuse scattering

Once the scattering results are acquired, it is fundamental to solve the average crystal structure from the Bragg peaks, which can be routinely carried out using well-established computer programs [29]. *A priori* knowledge of the atomic arrangement is imperative for subsequent modelling. Preliminary data about partial site occupancy and atomic displacement can also provide insights into the disorder [27].

To obtain a complete diffraction dataset in reciprocal space, images obtained from multiple orientations need to be reconstructed and symmetrised corresponding to the Laue group. With the capacity to survey large volumes of the reciprocal space, it becomes possible to process diffraction data directly to reveal the real-space distribution. By applying a Fourier transform (FT) to a total scattering dataset, the 3D pair distribution function (3D-PDF) can be obtained, which describes the probability of finding a pair of atoms separated by a certain vector in 3D. To avoid the average structure dominating the signals, it is often more useful to examine the FT of the DS, referred to as the 3D difference pair distribution function (3D-ΔPDF) [30]. This function reveals local deviations away from the periodic average, where a positive feature represents an excess of electron density at separations characterised by a certain vector, and a negative feature corresponds to reduced electron density. This method is explored in depth in Section 2.2.

Figure 1.4 shows the 3D-ΔPDF of some TE materials. In the 3D-ΔPDF of PbTe presented in (b), observed features were justified by a correlated anion–cation dimerisation and local dipole formation, likely underpinning the high TE performance of PbTe [31]. (c)–(f) are cross-sections of the DPs and the 3D-ΔPDF of defective half-Heusler $Nb_{1-x}CoSb$ synthesised under quenching and slow-cooling respectively. The Nb/vacancy disorder and associated Sb and Co relaxation were identified from these diagrams. The more localised diffuse peaks in (d) compared to (c), transformed to a slower decay of signal intensity in (f) than (e), implying longer-range correlation in slowly-cooled samples [32].

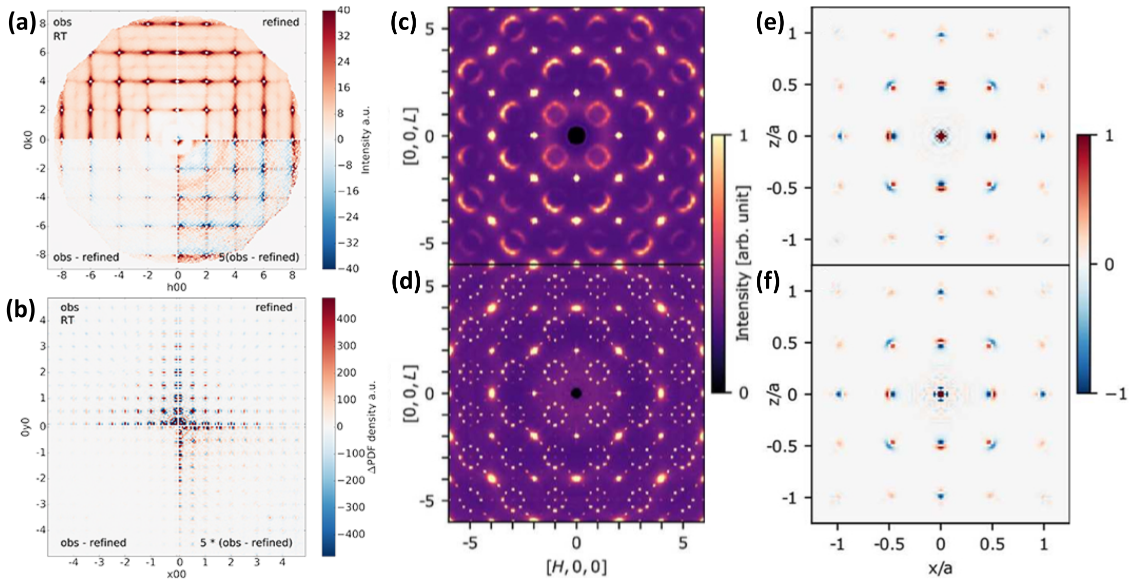

Figure 1.4. **(a)**–**(b)** X-ray DP in the [*H K* 0] plane and 3D-ΔPDF in the [1 1 0] plane of PbTe measured at room temperature, sourced from [31]. **(c)**–**(d)** X-ray DPs in the [*H* 0 *L*] plane for a quenched and a slowly-cooled sample of $Nb_{1-x}CoSb$ at 300 K. **(e)**–**(f)** Corresponding 3D-ΔPDF in the [0 1 0] plane, adapted from [32].

The 3D-ΔPDF methodology often serves as a diagnostic tool to unveil mostly a qualitative picture of the disorder. Solving the disorder eventually entails producing a real-space model structure based on this information, of which its calculated DPs exhibit a satisfactory match with those experimentally measured [21].

1.3.3 Modelling of diffuse scattering

Currently, one of the most commonly practised routines for modelling disorder is the MC simulation, an algorithm used to obtain low-energy configurations of disordered systems [33]. This algorithm is applied to a large box of particles representing the disordered system, and involves iterations of small changes, such as moving an atom or changing an atomic state, based on an established interaction potential using the Metropolis algorithm (*cf.* Section 2.3). The model can be adjusted until a satisfactory match is achieved between the DPs calculated from the generated configurations and the observed data [34]. Ever since its first application by Teller *et al.* in 1953 [35], MC simulations have been used to elucidate defect distributions in numerous materials, such as the vacancy/vacancy repulsion in aluminosilicate ceramic mullite [36], and the paracrystal array of defect clusters in the non-stoichiometric oxide, $Fe_{1-x}O$ [37].

To overcome the difficulty of proposing appropriate energy expressions, the reverse Monte Carlo (RMC) method is an alternative solution [38]. This method also refines a supercell of atoms using the Metropolis algorithm, to minimise, in this case, the goodness of fit. This parameter quantifies the difference between the calculated and experimental scattering intensities. However, the number of accessible degrees of freedom (DoFs) is very large for each step of the process. As such, RMC tends to produce many different, sometimes unphysical, configurations with equally good fits [38].

It is understandable if one questions the accuracy of the MC simulations, given that the interatomic interactions are greatly simplified and premised on an intuitive understanding of the system. It is also not uncommon for a range of MC models to yield similar results [21]. In response to these concerns, rigorous *ab initio* calculations have been progressively implemented over the years, driven by advancements in computational power. Techniques such as molecular dynamics (MD) and density functional theory (DFT) can provide accurate structural information based on precise classical or quantum mechanical calculations [39].

However, some of these *ab initio* methods come with considerable computational costs, limiting the number of atoms that can be processed. This is disadvantageous especially when a large enough system is needed to generate diffraction data comparable with experimental results [38]. Another challenge associated with these simulations is to identify the key physics at play. Simplified MC models can therefore be useful in probing the fundamental mechanisms of relevance to a particular problem. Even in cases where numerical accuracy is important, there are techniques like cluster expansion MC, which uses DFT to compute energies for large-scale MC simulations [40].

1.4 Thesis overview

The primary objective of this thesis is to revisit the local invariance model for occupational disorder in binary systems. This is a simple yet powerful model, providing a direct link between the shape of an observed diffuse distribution and the local crystal chemical constraints [21], which in the past required intensive manual calculation. The advancements in modern computing technology give us the opportunity to integrate it into MC simulations. By combining these individually powerful techniques, we aim to devise a generic strategy for studying binary systems with occupational disorder.

In this thesis, a MC algorithm was developed based on the local invariance energy model. In Chapter 3, this algorithm was validated by a simple 2D model; this model offered insights into the potential application of this algorithm in more complex systems. In Chapter 4, this algorithm was adapted to examine the local disorder in $V_{1+\delta}Sb$. SC-XRD measurements and average structure refinement were carried out. With the aid of Brillouin zone-averaging and 3D-ΔPDF, a model was constructed using a combined local invariance method and pair interaction method, to describe the occupational disorder of the vanadium/vacancy substructure. This model was subsequently improved to study the vacancy-induced Sb displacement. We aim to, through acquiring a thorough understanding of the local structure, deduce the potential of $V_{1+\delta}Sb$ for TE applications.

2

Methods

The general approach to studying disordered solids requires accurate modelling of atomic configurations that captures the key disorder responsible for the DS observed. The standard practice begins with predicting plausible modes of disorder, followed by generating representative configurations using appropriate simulation methods [41]. From these configurations, one can calculate the DS and 3D-ΔPDF for validation against experiment.

This chapter covers the key methods used in this study. First, the SC-XRD measurements used to characterise DS in $V_{1+\delta}Sb$, and the process of extracting 3D-ΔPDF from these data are detailed. Following this, a summary of MC methods for generating models of disordered systems, and an introduction of the local invariance approach, which is the core analytical strategy employed in our analysis, are provided. Towards the end of this chapter, a comprehensive example is given, illustrating the combined use of 3D-ΔPDF and MC simulations to understand the local invariance model.

2.1 Single-crystal X-ray diffraction measurement

In Section 1.3.1, we discussed some general aspects of DS measurements. For the SC-XRD measurement conducted in this thesis, the $V_{1+\delta}Sb$ single crystals used were synthesised by the Rosseinsky Group at the University of Liverpool. The measurement was performed at the Inorganic Chemistry Laboratory, University of Oxford using the XtaLAB Synergy diffractometer equipped with an EIGER R 1M pixel-counting detector.

The data-acquisition process involved two full 360° ϕ-rotation scans, with the detector positioned at $2\theta = 30^\circ$ and $2\theta = 70^\circ$, respectively. At each detector position, 720 frames were captured, with an exposure time of 100 s per frame. Mo Kα radiation ($\lambda = 0.71073$ Å) was used, and the measurement was conducted at an ambient temperature of 293 K.

The collected diffraction images were indexed and integrated using the *CrysAlisPro* software [42]. Average structure refinement was carried out using *JANA2006* [43]. 3D reconstruction and $6/mmm$ Laue class symmetrisation was performed using the program, *Meerkat* [44]. The results from these data treatments can be found in Section 4.1.

2.2 3D difference pair distribution function

The pair distribution function (PDF) is a common tool used in the analysis of diffraction data, especially for materials that have some degrees of disorder [41]. Standard PDF analysis typically involves a FT of the *powder* diffraction data, producing a 1D function. This function depicts the probability of finding a pair of atoms a certain distance apart, relative to the average expectation for a completely random distribution [45]. PDFs from *single-crystal* data are calculated as the FT either of the total scattering (total 3D-PDF) or of the DS alone (3D-ΔPDF) [46]. As discussed in Section 1.3.2, 3D-ΔPDF provides information about features of the real structure that are not represented by the average structure, and is thus more useful for analysing disorder [41].

The 3D-ΔPDF is a 3D *difference* map which provides a real-space representation of the interatomic vectors within a crystal. In this map, the signal at [**u**, **v**, **w**] corresponds to all pairs of atoms, indexed by *i* and *j*, separated by $\mathbf{u} = \mathbf{x}_i - \mathbf{x}_j$, $\mathbf{v} = \mathbf{y}_i - \mathbf{y}_j$, and $\mathbf{w} = \mathbf{z}_i - \mathbf{z}_j$ [47]. The intensity of the peaks is related to the difference between the conditional probability that if one site is occupied the connected site is also occupied, and the average occupancy [48]. Positive signals indicate that the corresponding pairs occur more frequently in the real structure compared to the average structure, while negative signals indicate the opposite. An example showing how ΔPDF can be interpreted to draw meaningful insights into the structural disorder is presented in Section 2.5.

Practically, to extract the DS from the diffraction data, the *punch-and-fill* method is often employed. In this method, the Bragg peaks are filtered by zeroing out all pixels in the close vicinity of the Bragg positions. Subsequently, these ’punched’ pixels are ’filled’ with estimates of the DS by extrapolation from surrounding pixels [49]. In our case, the measured DPs of $V_{1+\delta}Sb$ show little overlap between the Bragg peaks and the DS. Hence, the Bragg peaks were removed through spherical punches at reflection locations allowed by the $P6_3/mmc$ space group. The punched gaps were filled using the median intensity values drawn from nearby regions in reciprocal space. The isolated DS were Fourier transformed via a custom Python script, to produce the 3D-ΔPDF displayed in Figure 4.4.

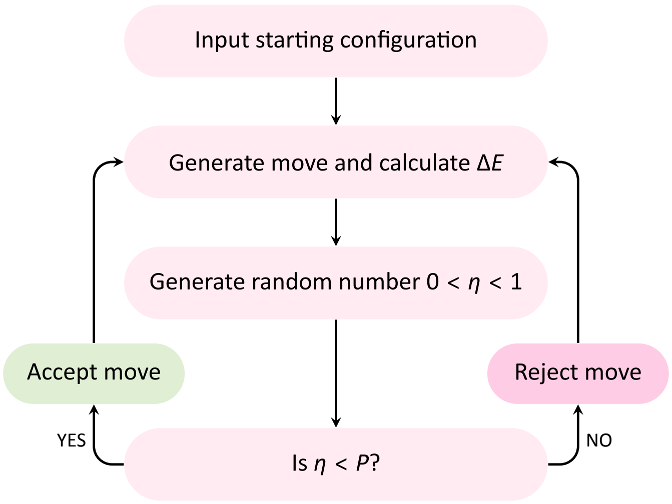

Figure 2.1. Flowchart for Metropolis–Hastings MC algorithm

2.3 Monte Carlo simulations

The MC method is one of the most popular techniques in solid-state modelling due to its simplicity and generality [33]. Typically, a supercell of atoms based on the composition and the lattice symmetry of the average structure is first generated, with periodic boundary conditions. Each atom is associated with some DoFs. For example, to investigate the vanadium/vacancy distribution in $V_{1+\delta}Sb$, the type of particle at each lattice site is the DoF of interest. An appropriate energy expression is then introduced based on the proposed SRO.

The simulation typically follows the Metropolis–Hastings algorithm, as illustrated in Figure 2.1. In this process, an atom selected at random from the supercell has its DoF changed at random based on a pre-set mechanism. To simulate a system with occupational disorder, this change can be a swap move between two nearest neighbours. The energy difference, ΔE, of the configuration before and after the move is calculated using the pre-determined interaction potential. The move is always accepted if the energy of the system is reduced. Otherwise, the move can be accepted if the transition probability (P), given by

$$P = \exp\left(-\frac{\Delta E}{T}\right), \tag{2}$$

is higher than a random number η chosen uniformly between 0 and 1 [50].

The parameter, T, functions as a control for accepting 'bad' moves, behaving as the thermodynamic temperature in the Boltzmann probability expression. It can be given a high initial value which decreases progressively for each MC cycle to simulate the process of annealing. The high-temperature perturbation allows exploration of a higher-energy landscape and transitions out of a local optimum [51]. T can also be given a constant low value, known as quenching, for faster convergence. Quenching can sometimes be applied preferentially if there is difficulty in finding a suitable cooling schedule, especially since it is possible for real systems to be trapped in metastable local states [52].

Trial moves are iteratively evaluated, being either accepted or rejected, which drives the system towards a predefined convergence condition. The simulation might be stopped, for example, once every site has been visited a large number of times and the system has reached equilibrium. To increase statistical reliability, MC simulations are repeated for different starting configurations. DPs are then computed using FT programs from sufficient configurations. In this thesis, the *Scatty* program was used for the calculation of DPs from the simulated atomistic models [53]. Since multiple MC simulations were performed in this work with different conditions, the specifics related to each simulation are detailed within their respective sections.

2.4 Local invariance model

The success of a MC simulation often hinges on defining an energy function to capture as far as possible relevant correlations present. The most commonly used Hamiltonian to model vacancy distributions in correlated disordered solids is the pair interaction approximation [50]. It assumes that pairwise interactions, typically those between nearest neighbours and next-nearest neighbours are dominant in SRO, while the higher-order interactions can be neglected. For instance, a model established to avoid nearest-neighbour vacancy pairs and minimise next-nearest-neighbour vacancy pairs in defective half-Heusler systems was found effective [52].

For occupational disorder, where atoms and/or vacancies are arranged on a sub-lattice of a larger structure, cluster-based modelling proves useful [24]. Assuming that the underlying lattice remains largely constant in different substitutional arrangements, cluster-based energy calculations can accommodate higher-order interactions with fewer DoFs involved [54]. Among the various cluster-based potentials, a simple but elegant method is built on the principle of local stoichiometric invariance. The basic idea is that the building blocks within the disordered sub-lattice should have stoichiometry as close as possible to the overall macroscopic composition of the sample [55].

This approach is based on the fundamental principle of Pauling's electroneutrality [56]. To maintain overall homogeneity and prevent phase separation within the crystal, electroneutrality should prevail at a local scale, despite the overall disorder. It was used to rationalise the vacancy SRO in substoichiometric Group IV and Group V transition metal carbides and nitrides, MC_{x-1} and MN_{x-1} [57], the evolution of the transition state of the

Ni–Mo and Au–V alloy systems [58], the ordering of Cu ions in Cu_xNbS_2 [59], and the oxygen and fluorine distribution $K_3MoO_3F_3$ [60].

It is a powerful method because the mathematical formulation of the local stoichiometric restriction sets constraints on the distribution of diffuse intensity in reciprocal space. Consequently, for a specific cluster type, the diffuse intensity can only exist along certain surfaces.

Herein, we provide a brief summary of the important steps involved in the mathematical derivation, for a lattice containing two distinct species, A and B. These species can either be two different elements or one element and vacancies, with atomic fractions m_A and m_B, respectively. The occupancy of species A of the site at position $\mathbf{r}_j$ is denoted by σ_j^A, which can only take the values of 1 or 0. To ensure stoichiometric invariance, a local cluster consisting of S lattice sites must satisfy

$$\sum_{j=1}^{S} \sigma_j^\mathrm{A} = m_\mathrm{A} S \,. \tag{3}$$

This criterion imposes constraints on the Warren–Cowley SRO parameter, α_{ij}. This parameter serves as a quantitative measure of the degree of local order between atom types i and j, such that a negative α_{ij} implies an attractive correlation, while a positive α_{ij} suggests repulsion [61].

Since α_{ij} is related to the diffuse intensity through a FT [27], it has been demonstrated that the derived α_{ij} transposes the local invariance constraints into the DS such that, the diffuse intensity can only sit on a geometric locus given by

$$\sum_{j=1}^{S} \exp(2\pi \mathrm{i} \mathbf{q} \cdot \mathbf{r}_j) = 0 \,, \tag{4}$$

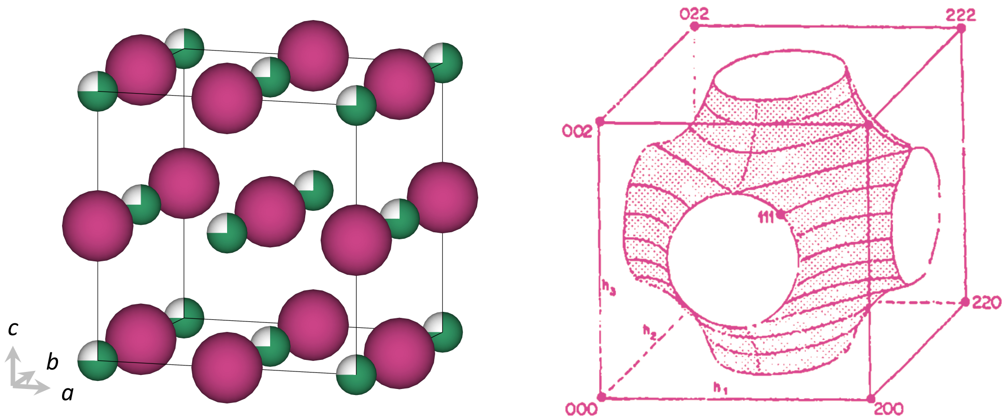

(a) (b)

Figure 2.2. **(a)** Average unit cell of $VC_{0.75}$, with V in purple and C in dark green. **(b)** Calculated diffuse intensity surface for octahedral local clusters, adapted from [58].

where **q** is the general vector in reciprocal space, and $\mathbf{r}_j$ is the position vector of the lattice point, *j*, within the cluster. The full derivation can be found in [58].

To elaborate on the concept, we examine an example drawn from literature, $VC_{0.75}$ [62]. This compound has a defective NaCl structure as shown in Figure 2.2 (a). C atoms partially occupy the octahedral sites of the FCC V array. The local invariance model requires C atoms to be arranged around each V atom such that, three-quarters, or four to five of the six octahedral sites should be occupied.

Substitution of the lattice point coordinates of an octahedral local cluster into Equation (4) yields the intensity surface, also known as the Schwarz *P* minimal surface [63],

$$\cos(\pi h) + \cos(\pi k) + \cos(\pi l) = 0\,. \tag{5}$$

Figure 2.2 (b) offers a visual representation of this surface in 3D.

A comparison of the measured electron DPs with the corresponding calculated diffuse intensity in selected cross-sections is shown in Figure 2.3. A clear consistency can be seen not only in the listed planes but also across the entire 3D reciprocal space; hence,

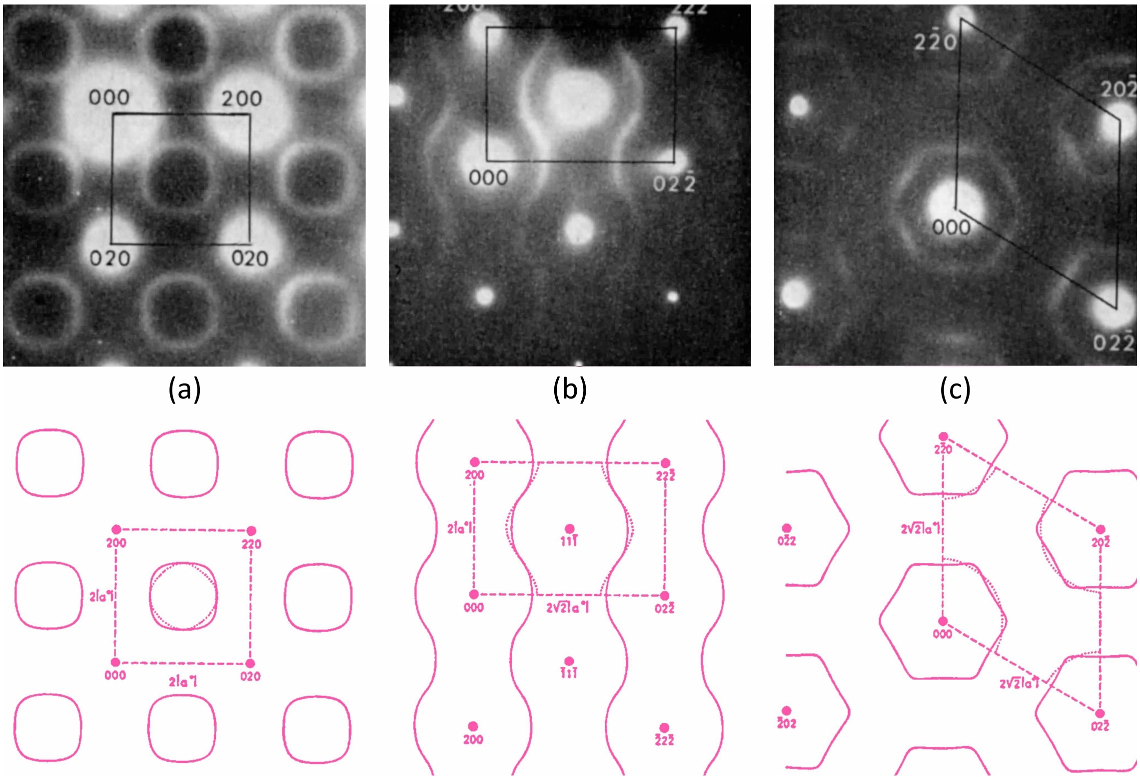

(a) (b) (c)

(d) (e) (f)

Figure 2.3. (a)–(c) Electron DPs in the [001], [011], and [111] cross-sections of $VC_{0.75}$, sourced from [62]. **(d)–(f)** Corresponding calculated DS, adapted from [57].

the local invariance model succeeds in rationalising occupational disorder in binary solid systems. Given the similar type of disorder in $V_{1+\delta}Sb$, this model is used in Chapter 4.

2.5 An example

To illustrate how 3D-ΔPDF could provide a straightforward interpretation of the local correlation, a set of simple simulations were shown in Figure 2.4. The simulated 'crystal' sits on a 2D square lattice, with a primitive unit cell of length 3.0 Å. In each of the 20 × 20 supercells, 70% of the lattice sites are occupied by Fe atoms, leaving the rest vacant. MC simulation was conducted using the local invariance model, where the Fe atoms arrange themselves such that the occupancy of all smallest square clusters within the structure aligns as closely as possible with the overall composition.

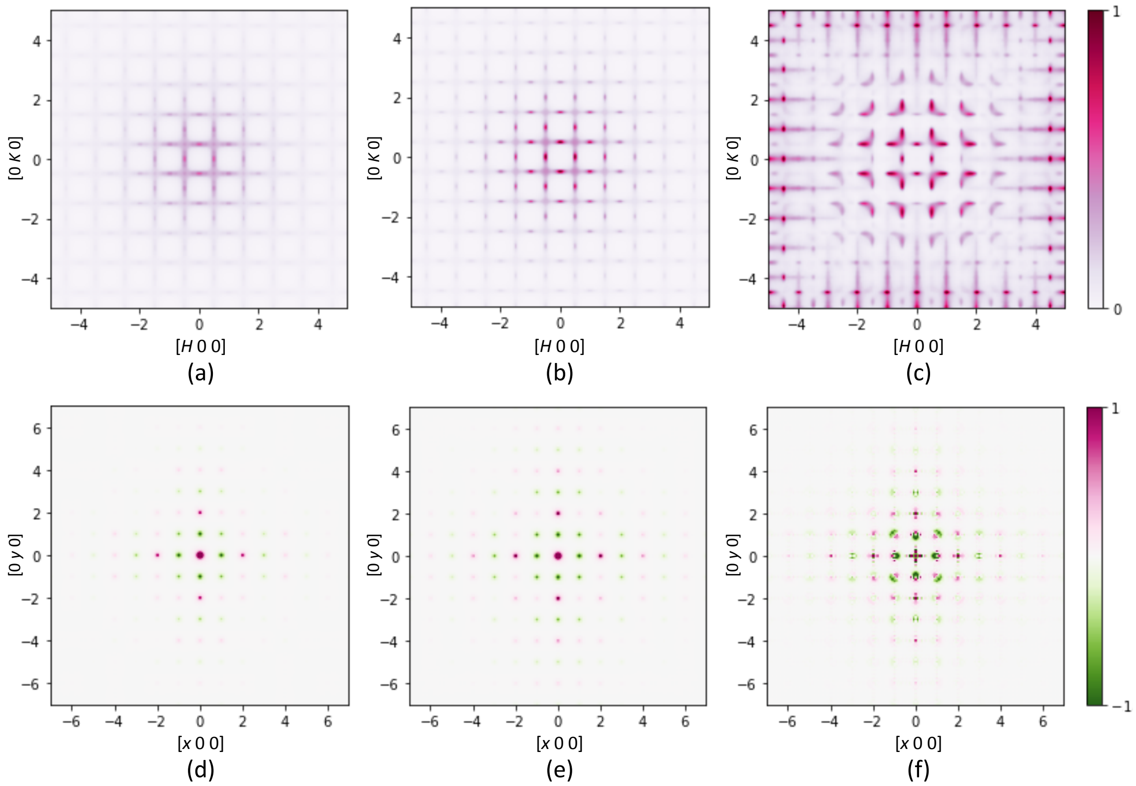

(a) (b) (c)

(d) (e) (f)

Figure 2.4. **(a)**–**(c)** Simulated X-ray DS patterns of a binary 2D square lattice with occupational disorder and shorter-range order, occupational disorder and longer-range order, and size effect disorder, respectively. **(d)**–**(f)** Corresponding 2D-ΔPDF.

Simulations were conducted for three different disorder conditions. The DPs obtained from a collection of 20 MC configurations are shown in the top row of Figure 2.4, and the corresponding 2D-ΔPDF are shown in the bottom row. Since all structures have, on average, 0.7 Fe atoms sitting on every lattice site, they yield identical Bragg peaks which were removed from the DPs. The left and middle columns are examples of purely occupational disorder, while the last column illustrates the *size effect* modulation, or in other words, displacive disorder arising from neighbouring vacancies [46].

Details about the occupational disorder can be obtained by examining the 3D-ΔPDF shown in (d) and (e). The positive peak at the origin suggests a positive correlation with the atom itself. The four nearest-neighbour negative signals at $[\pm1, 0]$ and $[0, \pm1]$

imply a lower-than-average probability for lattice sites separated by those vectors to be both occupied by Fe. The four next-nearest-neighbour signals at $[\pm1, \pm1]$ are also weakly negative. This is because the square clusters encompass both nearest-neighbour and next-nearest-neighbour Fe–Fe pairs, while the former occurs twice more within a cluster. The local invariance model thereby avoids both nearest- and next-nearest-neighbour Fe–Fe pairs. The surrounding positive signals at $[\pm2, 0]$ and $[0, \pm2]$ then suggest a higher tendency for Fe–Fe pairs to be separated by those vectors. This is consistent with diffuse streaks appearing at half-integer H and K positions in DPs (a) and (b), both suggesting a correlation length twice that of the length of the unit cell.

The key difference between the first two columns lies in their respective simulation 'temperatures'. Although both simulations were quenched, the T value used for the simulation in the left column was four times higher. As a result, the final configurations generated for the left column were more disordered. This means that the correlated site occupations become increasingly random at larger distances, so the correlation length is shorter and the 3D-ΔPDF signals are less extended in (d) [48]. The broader DS in (a) as compared to (b) conveys the same information, since the width of diffuse features is inversely proportional to the correlation length of local order [27].

The advantages of 3D-ΔPDF become clearer when interpreting size effects. While the presence of size effect can be identified in Figure 2.4 (c) from the asymmetric DS [64] around the Bragg positions, details about the disorder are hard to be extracted directly.

Figure 2.5 (a) illustrates the vacancy-induced Fe displacement employed in the simulation for the last column of Figure2.4. If there is a vacancy in one of the nearest-neighbour sites of a Fe atom, the Fe atom moves towards the vacancy, as demonstrated by the atoms A

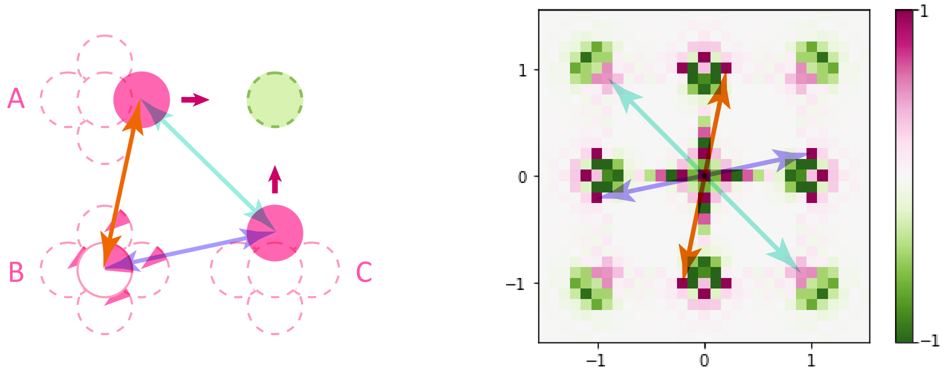

(a)

(b)

Figure 2.5. **(a)** Diagram showing vacancy-induced splitting of Fe atoms (pink) towards a vacancy (green). **(b)** A magnified portion of Figure 2.4 (f).

and C. Assuming that atom B is at its average position, there is then a higher-than-average probability of observing the Fe–Fe pair separated by vectors in purple and orange. This gives rise to the features found around [±1, 0] and [0, ±1] in (b). These signals are negative towards the centre, with three surrounding positive peaks. One set of positive peaks, indicated by the purple and orange arrows, can be explained by the situation presented in (a). The rest of the positive signals can be explained by analogue cases with different vacant sites (e.g. below or to the right of atom C).

At around [±1, ±1], a positive region is seen towards the centre, which can be explained by the increased probability of two next-nearest neighbours, exemplified by atoms A and C in Figure 2.5 (a), moving closer to each other when they shift towards the same vacancy (the blue arrows). It is worth noting that the integrals of the surrounding signals at [±1, ±1] are negative. This aligns with the negative signals at [±1, ±1] in Figure 2.4 (d) and (e) since all simulations shared the same correlation in occupational disorder.

These examples demonstrate that for structures with the same average unit cell, the 3D-ΔPDF, which transforms abstract reciprocal correlation into real space, can serve as an invaluable tool for identifying and understanding different SRO.

3

2D local invariance model

The first objective of this project is to explain the behaviour of the local invariance model on two high-symmetry lattices — square and hexagonal — as a simplified model system of conceptual relevance to $V_{1+\delta}Sb$. In this chapter, MC simulations were performed on square and hexagonal binary systems using potentials derived from the local invariance rule for a number of different cluster types.

3.1 Single cluster

A 20 × 20 supercell comprising two elements in a predetermined ratio was first generated, with random distribution. For the i^{th} local cluster of a specific shape, its fractional composition is denoted as s_i. The energy of the starting configuration was determined by evaluating the sum of the squared difference between s_i and the overall composition of the lattice, s, for all N local clusters found within the configuration, according to

$$E = \sum_{i=1}^{N} (s_i - s)^2 \,. \tag{6}$$

The value of E was minimised whenever the composition of these local clusters is as close as possible to the overall composition. Small squares, large squares, and irregular

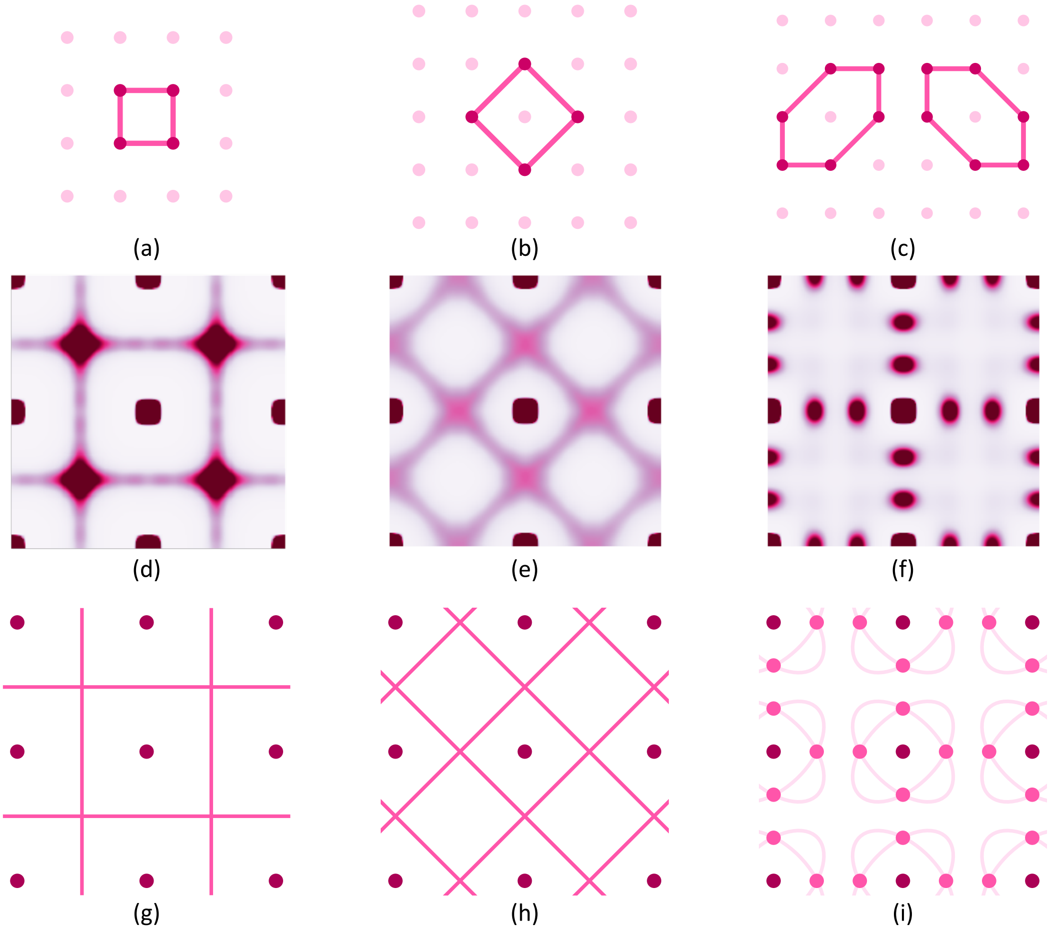

Figure 3.1. **(a)**–**(c)** Illustrations of the shapes of small square, large square, and hexagonal local clusters on a square lattice. **(d)**–**(f)** Corresponding DPs from MC simulations. **(g)**–**(i)** Plots of permissible diffuse intensity loci calculated from Equation (4).

hexagons were used as the local clusters for the square lattice; triangles, rhombuses, and regular hexagons for the hexagonal lattice. Illustrations of the shapes of these clusters can be found in the top rows of Figure 3.1 and 3.2.

Once a random starting configuration was generated, MC simulations proceeded with the aforementioned energy expression. The MC steps involved swap moves, wherein a particle at a random site was chosen and exchanged with one of its nearest neighbours, following the Metropolis algorithm introduced in Section 2.3 until the system converged. This process was carried out using a custom Python code. An ensemble of 20 MC

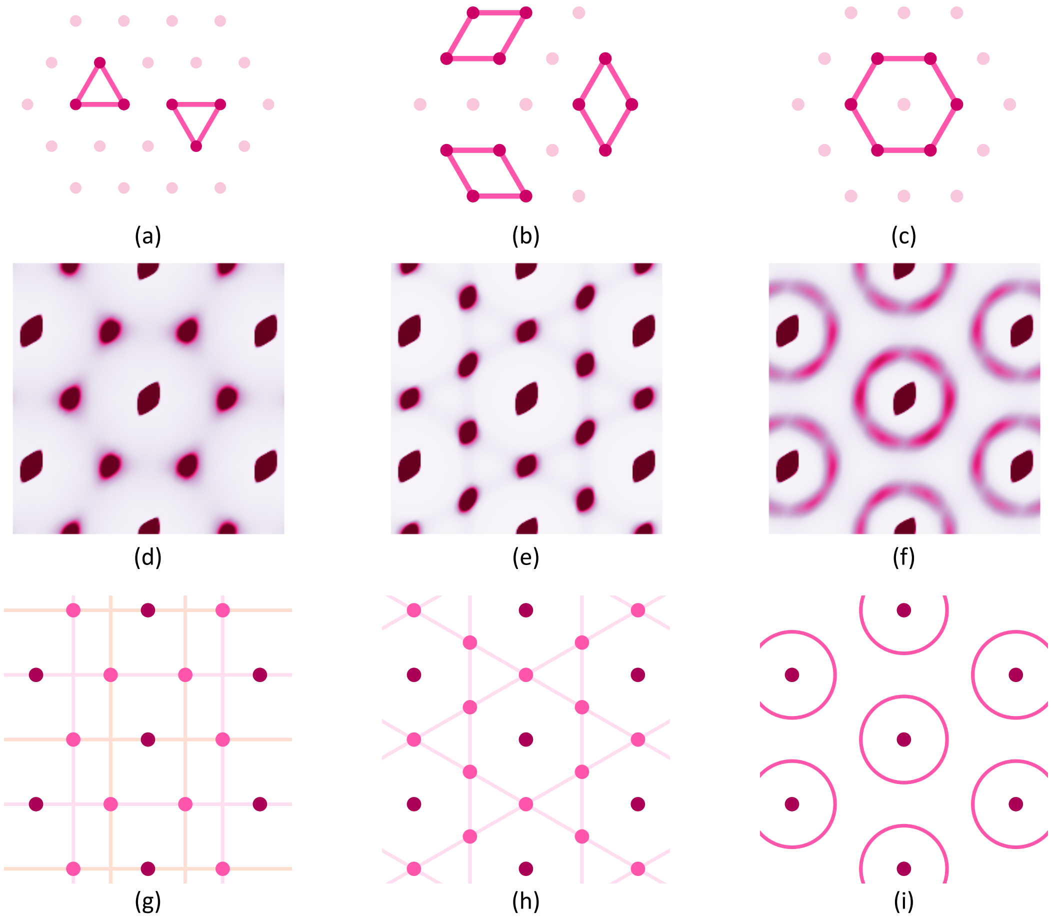

(a) (b) (c) (d) (e) (f) (g) (h) (i)

Figure 3.2. (a)–**(c)** Illustrations of the shapes of triangular, rhombic, and hexagonal local clusters on a hexagonal lattice. **(d)**–**(f)** Corresponding DPs from MC simulations. **(g)**–**(i)** Plots of permissible diffuse intensity loci calculated from Equation (4).

configurations was generated for computing each diffraction image, using the program *Scatty* [53].

The DPs derived from each cluster type were first simulated, setting the occupancy of the two elements to be equal. The resulting DPs are displayed in the middle row of Figures 3.1 and 3.2. Expressions for the allowed diffuse intensity loci were calculated using Equation 4 and depicted graphically at the bottom; the equations are given in Appendix A. In these graphical depictions, dark pink dots mark the locations of the Bragg peaks. For cluster types with more than orientations, multiple equations were produced, and their

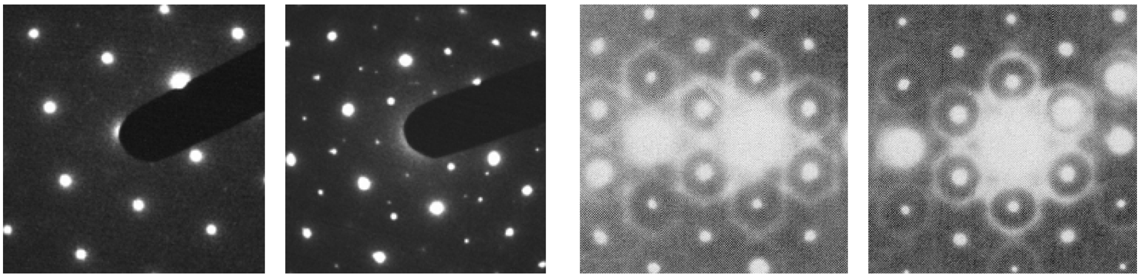
(a) (b) (c) (d)

Figure 3.3. **(a)**–**(b)** Electron DPs of $Cu_xBi_2Te_2Se$ when $x = 0$ and $x = 0.12$ in the $[H\,K\,0]$ plane, sourced from [65]. **(c)**–**(d)** X-ray DPs of Cu_xNbS_2 when $x = 0.5$ and $x = 0.75$, sourced from [59].

points of intersection are marked by light pink dots.

The remarkable similarity between the simulated DPs and the calculated intensity loci suggests that the cluster description of the binary occupational SRO is consistent with the mathematical formulation of the Warren–Cowley SRO parameter introduced in Section 2.4. More crucially, these simulations imply that an examination of the geometry of the DS alone could offer clues into the predominant clusters, and thus the nature of the local chemical constraints. A primary understanding of the predominant cluster type can offer insights such as the electronic driving force for ordering, and changes in packing behaviours due to changes in the composition of the binary system, etc.

Here, we present a comparative analysis involving real-world examples. Figure 3.3 (a) and (b) are the DPs of $Cu_xBi_2Te_2Se$ when $x = 0$ and $x = 0.12$, respectively, within the $[H\,K\,0]$ reciprocal plane. When $x = 0$, the Bi_2Te_2Se parent compound has a quintuple-layer structure, comprised of hexagonal layers stacked in the sequence of Te-Bi-Se-Bi-Te. When $x = 0.12$, Cu enters as an intercalant into the van der Waals gaps. In the original research, the emergence of additional peaks following the Cu intercalation was attributed to potential stacking faults or superlattice formation [65]. A resemblance can be observed

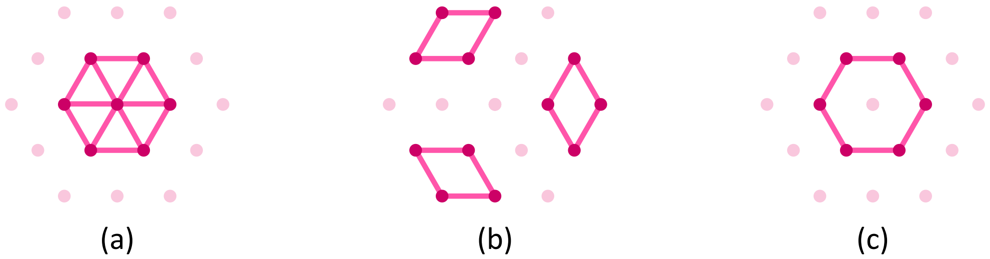

Figure 3.4. **(a)** Illustration of the 7-point cluster proposed in [59]. **(b)**–**(c)** Rhombic and hexagonal clusters for comparison.

between Figure 3.3 (b) and Figure 3.2 (d). This suggests that the emergent peaks could be potentially explained by correlated occupational disorder between Cu and vacancies on a hexagonal lattice within the intercalation layer. The relatively localised diffuse spots might result from a relatively ordered version which follows the same triangular invariance rule, leading to superlattice formation as postulated.

Figure 3.3 (c) and (d) are the DPs of Cu_xNbS_2 when $x = 0.5$ and $x = 0.75$, respectively. Cu_xNbS_2 has a hexagonal structure, built up from edge-sharing NbS_2 trigonal prisms layers, intercalated by Cu ions. In the original research, the transition in the shape of DS as the concentration of Cu increased, was explained by a 7-point cluster model, shown in Figure 3.4 (a). In the model, a composition-dependent parameter was included in the DS locus expression to explain the changes in DS observed [59]. Here, similarity is observed between Figure 3.3 (c) and (d), and Figure 3.2 (e) and (f), respectively. The DS in Figure 3.3 (c), despite not being localised at the intersections like in Figure 3.2 (e), still lies on the calculated locus. This leads us to hypothesise that as the composition of Cu increased, more hexagonal than rhombic clusters might be found to have the same stoichiometric composition as the overall structure. Given that both the rhombic and the hexagonal clusters are subcomponents of the proposed 7-point cluster, one might speculate that at certain compositions, the locally invariant distribution of atoms within all 7-point clusters can result in some smaller clusters fulfilling the local invariance rule, too.

3.2 Competing clusters

Seeing how a change in binary composition can trigger a transition in the predominant cluster types, further investigation was conducted to examine the effect of competing clusters on DS, with the modified energy expression,

$$E = \sum_{k=1}^{3}\Big(J_k \cdot \sum_{i=1}^{N_k}(s_{ik} - s)^2\Big). \tag{7}$$

In this expression, weighting coefficient, J_k, is assigned to each of the three cluster types for each lattice type, quantifying the relative importance of the respective cluster type. The parameters, s_{ik} and N_k, are the fractional composition of a local cluster and the total number of local clusters within the configuration, for cluster type k respectively. The overall composition of the configuration is again denoted as s, and has a fixed value between 0 and 1. The total energy of the configuration is then the sum of the energy contributed from all three cluster types.

MC simulations over a range of J_k ratios were performed, and the first Brillouin zones of the resulting DPs were presented in maps, shown in Figure 3.6 (a) and (b). J_1, J_2, and J_3 are the coefficients assigned to small squares, large squares, and hexagons for the square lattice; and to triangles, rhombuses, and hexagons for the hexagonal lattice.

Additionally, the *boundary accessibility* of the simulated configurations was calculated. Similar to porosity, this concept involves counting particles that can be reached from the top and left supercell boundaries by taking the nearest neighbours of the same type, ex-

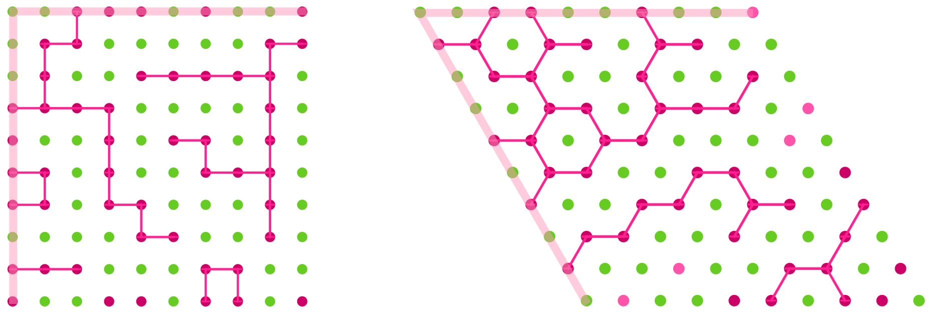

Figure 3.5. Illustration of boundary accessibility with boundary-accessible pink dots connected by lines. Periodic boundary condition applies and particles are taken from the left and top edges as highlighted.

pressed as a percentage of the total number of these particles. Graphical representations of the boundary accessibility pathways can be found in Figure 3.5. The accessibility was calculated by dividing the number of pink dots connected by the pink lines by the total number of pink dots in the configuration.

For every set of J_k ratios, the boundary accessibility was calculated for each of the 20 configurations used to compute the DP. The average of these values was taken and presented in maps shown in the lower section of Figure 3.6. Given that each particle in the hexagonal lattice has six neighbours, the boundary accessibility tends to be higher and displays less variation across different J_k combinations. To more effectively demonstrate the variations in boundary accessibility, the proportion of the pink dots was adjusted to 0.4 for the hexagonal lattice, while maintained at 0.5 for the square lattice.

Phase crossovers are observed in the DP maps, as the ratio of J_k varies, evident by changes in shapes of the DS. Notably, these phase crossovers are also associated with changes in boundary accessibility. In other words, different types of clusters tend to foster different correlations in arrangements of particles, which can in turn affect certain physical properties. Sample configurations at three specific J_k ratios are shown for the square lattice

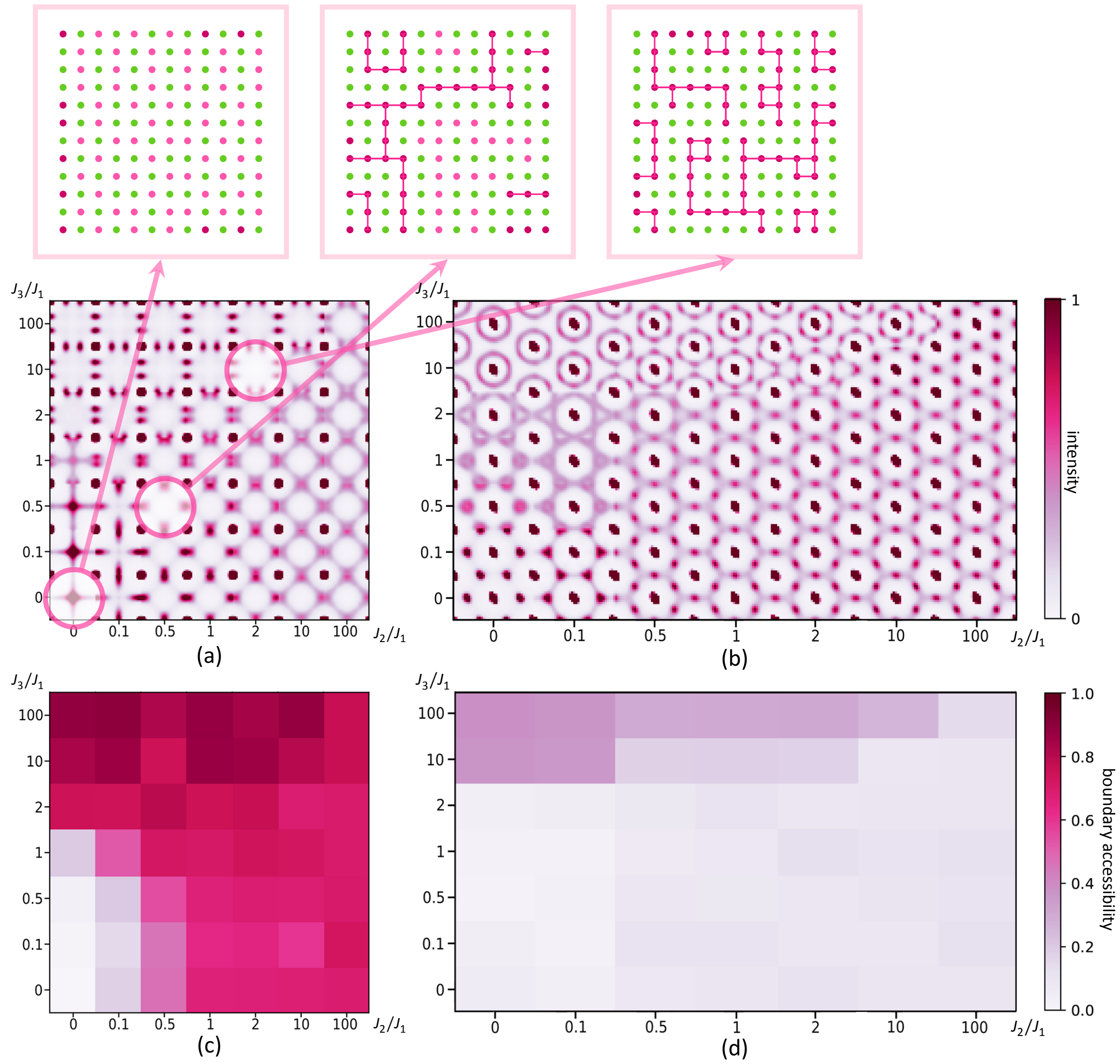

Figure 3.6. **(a)–(b)** DP maps plotted against different J_k ratios for square and hexagonal lattices, respectively. **(c)–(d)** Corresponding boundary accessibility maps. J_1, J_2, and J_3 correspond to small squares, large squares, and hexagons in the square lattice; and to triangles, rhombuses, and hexagons in the hexagonal lattice, respectively.

at circled positions in Figure 3.6 (a). For example, at the bottom left, when both J_2 and J_3 are zero, the MC energy optimisation is based solely on small square clusters. This results in a preference for an alternating particle arrangement, thereby leading to extremely low boundary accessibility.

Despite the simplicity of this 2D local invariance MC simulation, several implications can be drawn. First, a change in the dominant cluster type can result in phase crossovers which can potentially affect certain functional properties — particularly those associated with particle distribution and transport. As a result, phase maps as a function of J_k can be constructed for real materials exhibiting similar binary occupational disorder. The DS of structures with optimal functional performance can be identified from these maps and used as a guide for designing structurally-similar materials. Second, based on the examples presented earlier in this chapter, changes in composition could potentially trigger changes in the dominant cluster and therefore DS. Conversely, an analysis of the shape of the DS as the composition varies might provide insights into the particle arrangement.

4

Correlated disorder in $V_{1+\delta}Sb$

Sb-based materials are recognised for their high TE performance as discussed in Section 1.2. Group V metals are characterised by having high melting points, mechanical strength, electrical conductivity and corrosion resistance [66]. Although less explored, $V_{1+\delta}Sb$ is of particular interest to us, as we hypothesise that the disordered vanadium/vacancy network could play an important role in reducing the lattice thermal conductivity of the material, thereby enhancing its TE performance. The focus of this chapter is on the characterisation of local disorder in $V_{1+\delta}Sb$.

4.1 Single-crystal X-ray diffraction results

4.1.1 Average structure of $V_{1+\delta}Sb$

Details about the SC-XRD experiment and refinement is presented in Section 2.1. The $V_{1+\delta}Sb$ crystal is identified as hexagonal, with the $P6_3/mmc$ space group. The cell lengths, $a = 4.2794(1)$ Å and $c = 5.4491(1)$ Å, lie between the reported values for VSb [67] and V_3Sb_2 [68]. The data exhibited high quality, with an internal agreement (R_{int}) of 3.27% and a minimum d-spacing (d_{min}) of 0.39 Å. Other data from the average structure refinement

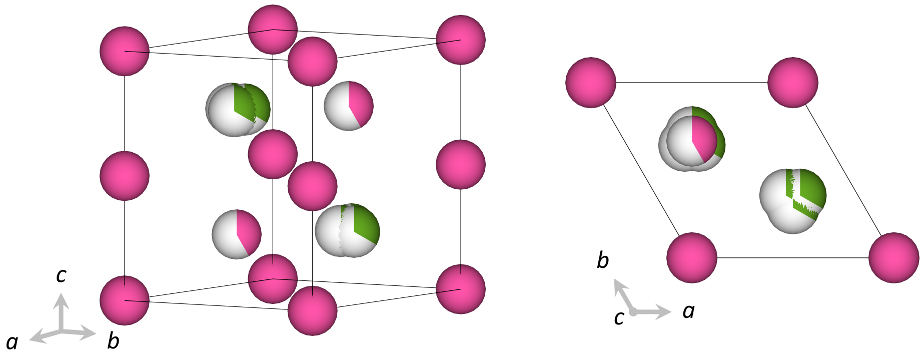

Figure 4.1. Average unit cell of $V_{1+\delta}Sb$ from different perspectives, with V in pink and Sb in green.

Chemical formula	$V_{1.424}Sb$	μ (mm^{-1})	11.021
Space group	$P6_3/mmc$	$(\sin\theta/\lambda)_{max}$ ($Å^{-1}$)	1.28
T (K)	293	$N_{Tot,obs}$	7629
a (Å)	4.2794(1)	$N_{Uniq,obs}$	319
c (Å)	5.4491(1)	$N_{Parameters}$	13
V ($Å^3$)	86.421(3)	R_{int}	0.0327
Z	2	R_1	0.0633
ρ ($g\,cm^{-3}$)	3.6266	wR_2	0.0939

	Sb	**V1**	**V2**
Position	[0.3567(6), 0.6433(6), 0.25]	[0, 0, 0]	[0.66667, 0.33333, 0.25]
Site	6h	2a	2d
Mult.	6	2	2
Occ.	0.3333	1	0.424(13)
U_{11} ($Å^2$)	0.0192(7)	0.01250(16)	0.0084(5)
U_{22} ($Å^2$)	0.0192(7)	0.01250(16)	0.0084(5)
U_{33} ($Å^2$)	0.00730(18)	0.0108(3)	0.0104(7)
U_{12} ($Å^2$)	0.0113(5)	0.00625(8)	0.0042(2)
U_{13} ($Å^2$)	0	0	0
U_{23} ($Å^2$)	0	0	0

Table 4.1. Crystallographic data from the average structure refinement of $V_{1+\delta}Sb$

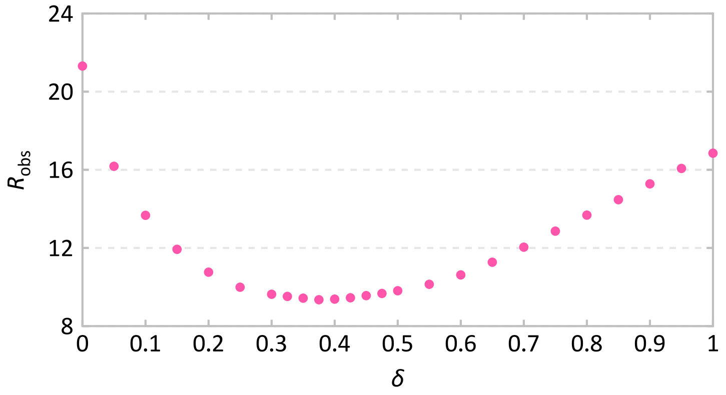

Figure 4.2. Dependence of R_{obs} on the modelled occupancy of V2 (δ)

can be found in Table 4.1.

In the ideal structure, Sb atoms locate at [1/3, 2/3, 1/4] and symmetry-related positions. A stoichiometric amount of V atoms (denoted as V1) are positioned at [0, 0, 0] and equivalents, while the excess V atoms (denoted as V2) are at [2/3, 1/3, 1/4] and equivalents. The V1Sb substructure resembles that of NiAs; with the V2 atoms partially occupying the trigonal prismatic sites. Sb and V2 form interpenetrating hexagonal close-packed (HCP) networks, in between layers of primitively arranged V1 atoms.

Since residual electron density was found around the ideal positions of Sb, further refinement was carried out by slightly displacing Sb from its central position. Following this, a notable improvement was observed in R_{obs}, suggesting a better agreement between the observed and refined data. As a result of this refinement, each Sb atom is split into three positions each pointing towards one of the in-plane V2/vacancy neighbours as depicted in Figure 4.1. Detailed information regarding the atom positions and anisotropic displacement parameters (ADPs) can be found in the lower section of Table 4.1.

The refinement suggested a V2 occupancy of 0.424(13). To enhance the accuracy, we conducted another series of refinements, holding V2 occupancy constant at different values while allowing all other parameters to freely adjust. The resulting R_{obs} were plotted against their respective occupancy values, as shown in Figure 4.2. R_{obs} is reasonably low and stable when δ is in the range of 0.3–0.5. This aligns with a previous research finding that NiAs-type $V_{1+\delta}Sb$ has an existence region around the composition of $V_{1.40}Sb$ [69]. Thus, $\delta = 0.4$ is used for subsequent simulations.

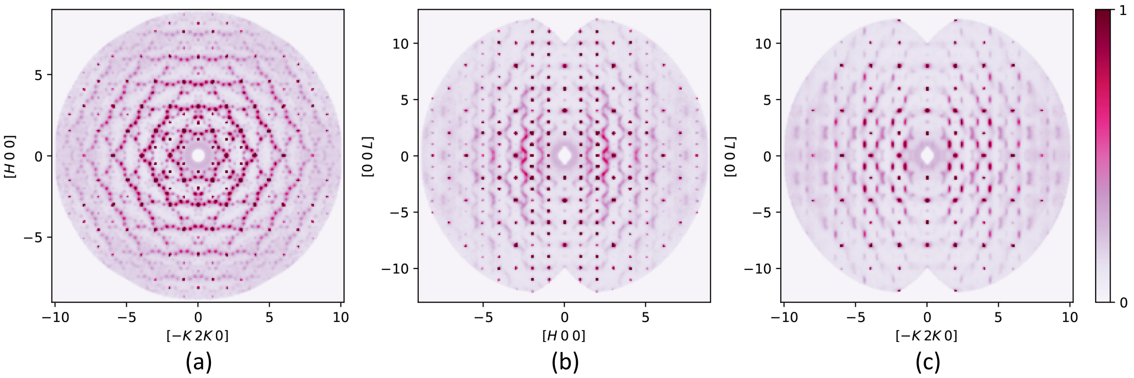

Figure 4.3. Reciprocal-space reconstructed SC-XRD data of $V_{1+\delta}Sb$ measured at 293 K in the **(a)** [*H K* 0], **(b)** [*H* 0 *L*], and **(c)** [–*K* 2*K L*] planes.

4.1.2 Diffraction patterns of $V_{1+\delta}Sb$

Selected cross-sections of the reciprocal-space reconstructed DPs are shown in Figure 4.3. In the [*H K* 0] plane shown in (a), besides the fundamental Bragg peaks, prominent diffuse spots can be seen. These diffuse spots predominantly occur in a hexagonal arrangement encircling the Bragg position; while there is a noticeable asymmetric intensity modulation attributable to the size effect. In (b), the [*H* 0 *L*] plane contains continuous diffuse waves between columns of Bragg peaks along the [0 0 *L*] direction. Notably, phase changes in these diffuse waves are seen between columns with $H = 3$ and 4, and with $H = 6$ and 7. The [–*K* 2*K L*] plane shown in (c) is mutually perpendicular to [*H K* 0] and [*H* 0 *L*]. This plane exhibits systematic absences along the [0 0 *L*] direction which corresponds to the same feature in the [*H* 0 *L*] plane when *H* is an integer multiple of three. Pairs of diffuse spots, elongated along the [0 0 *L*] axis, are found between rows of Bragg peaks. Additionally, another set of less intense diffuse features appears on the same rows as the Bragg peaks.

In broad terms, the presence of structured DS suggests that the disorder within $V_{1+\delta}Sb$ is not random, but exhibits some forms of order. Based on the asymmetric DS, we anticipate that in $V_{1+\delta}Sb$, occupational modulations are coupled to atomic displacement.

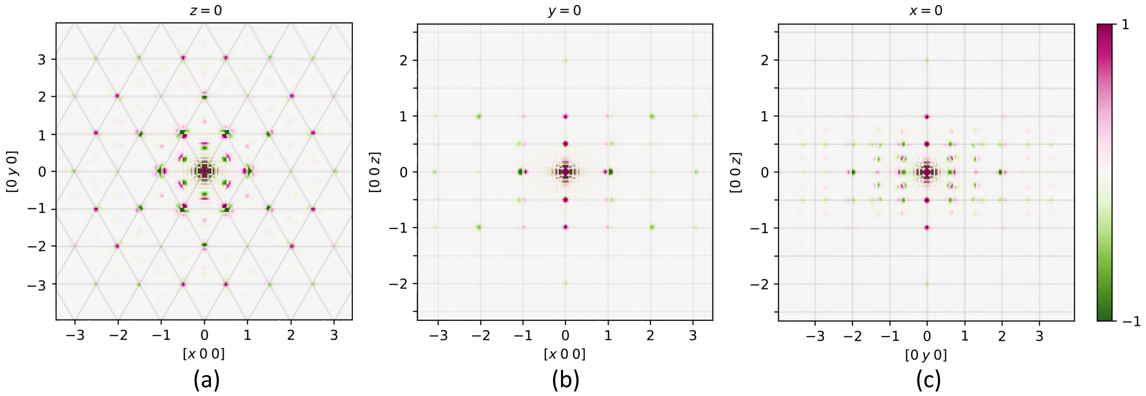

(a) (b) (c)

Figure 4.4. 3D-ΔPDF of $V_{1+\delta}Sb$ calculated from the measured diffraction dataset in the **(a)** [*x y* 0], **(b)** [*x* 0 *z*], and **(c)** [0 *y z*] planes. Basis vectors are defined using the Cartesian coordination system for easier interpretation.

4.1.3 3D-ΔPDF of $V_{1+\delta}Sb$

The 3D-ΔPDF was calculated using the punch-and-fill and FT methodology detailed in Section 2.2. A brief examination of the 3D-ΔPDF shown in Figure 4.4 reveals various forms of disorder. In the [*x y* 0] layer shown in (a), the dipolar component at [1/2, 1/3, 0], the quadrupolar component at [1/2, 1, 0], and the monopolar component at [1/2, 3, 0] suggest respectively the presence of size effect, correlated displacement, and occupational disorder within the plane [46]. In (b) and (c), the dipolar size effect features and quadrupolar correlated displacement features are predominantly split in the [*x* 0 0] and [0 *y* 0] directions, while the disorder along the [0 0 *z*] direction is mostly occupational. This suggests a primarily in-plane, vacancy-induced relaxation, consistent with the refined average structure.

The strong and asymmetric DS, and complex features in the 3D-ΔPDF together underscore the presence of occupational disorder with SRO and vacancy-induced relaxation. Consequently, addressing the disorder within $V_{1+\delta}Sb$ involves two steps — identifying the vacancy distribution, and determining the mode of relaxation.

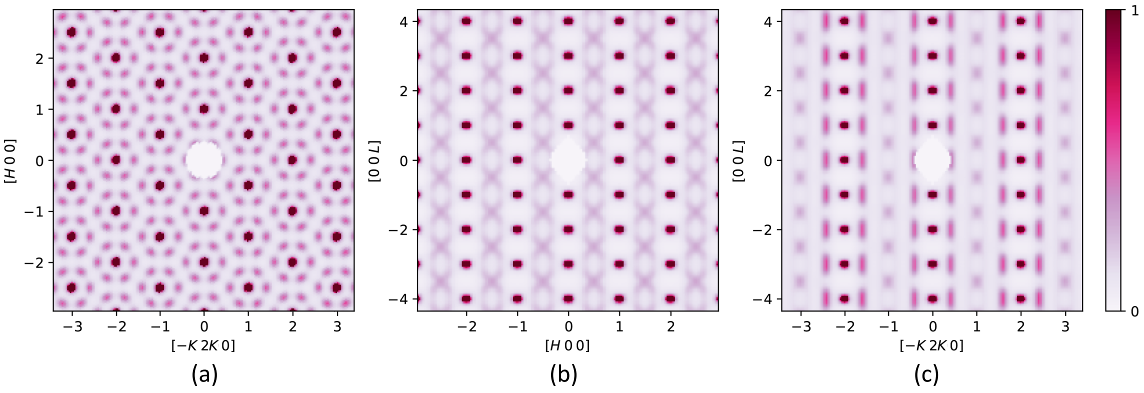

Figure 4.5. Brillouin zone-averaged DPs from the measured SC-XRD of $V_{1+\delta}Sb$ at 293 K in the **(a)** [*H K* 0], **(b)** [*H* 0 *L*], and **(c)** [–*K* 2*K L*] planes.

4.2 Occupational disorder in $V_{1+\delta}Sb$

4.2.1 Brillouin zone averaging

Research has shown that a novel technique, known as *Brillouin zone averaging*, has the ability to isolate occupational disorder effects on the diffuse intensity from all other disorder effects. This is achieved by a weighted projection of all diffuse intensity into a single reciprocal unit cell [70].

Brillouin zone averaging was applied to the diffraction dataset, using a Python script written by Nikolaj Roth. In this process, the measured diffraction dataset underwent a sequential shift, one reciprocal unit cell at a time, along the three reciprocal axes, with a circular boundary condition. During each shift, the diffuse intensity in every Brillouin zone was summed up. The resulting data, now devoid of size effect modulation, is illustrated through selected cross-sections in Figure 4.5. Successful recovery of the V2/vacancy distribution within $V_{1+\delta}Sb$ entails generating structures which yield DPs identical to the Brillouin zone-averaged images.

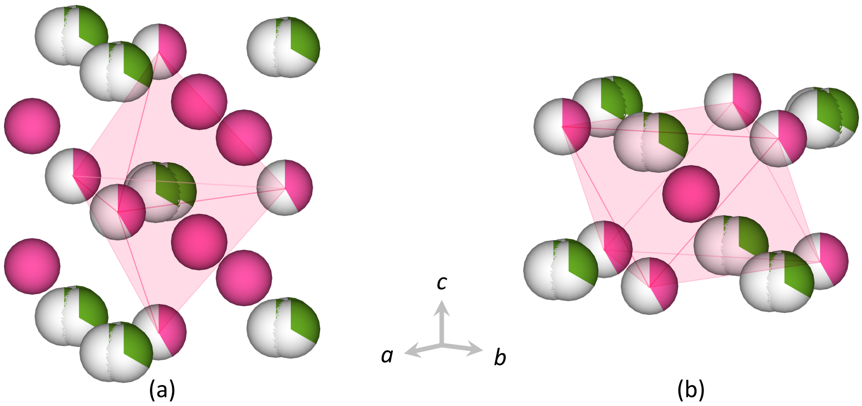

Figure 4.6. Diagram showing the local coordination environment in $V_{1+\delta}Sb$, depicting the V2/vacancy sites coordinating **(a)** the Sb atoms trigonal bipyramidally, and **(b)** the V1 atoms octahedrally.

4.2.2 Local invariance model

We first approached solving the V2/vacancy distribution by employing the local invariance model. In this case, the HCP network of V2 atoms and vacancies was considered as a binary system. Local clusters were defined based on the coordination of V2/vacancy sites relative to the ordered V1Sb sub-lattice. As highlighted in Figure 4.6, V2/vacancy sites coordinate around the Sb atoms and the V1 atoms in trigonal bipyramidal and octahedral manners, respectively. Both the trigonal bipyramids and the octahedra are face-sharing in the extended structure.

The local invariance potential comprises two components, each responsible for distributing V2 within the trigonal bipyramidal and the octahedral clusters, expressed as

$$E = J_{\mathrm{oh}} \sum_{i=1}^{N_{\mathrm{oh}}} (s_{\mathrm{oh},\,i} - s)^2 + J_{\mathrm{tbp}} \sum_{j=1}^{N_{\mathrm{tbp}}} (s_{\mathrm{tbp},\,j} - s)^2 \,. \tag{8}$$

In this equation, s and $s_{\mathrm{oh},\,i}$ denote the overall proportion of V2 in the V2/vacancy HCP configuration, and the fractional occupancy of V2 in the i^{th} octahedral cluster. The sum encompasses all N_{oh} octahedral clusters and N_{tbp} trigonal bipyramidal clusters, each as-

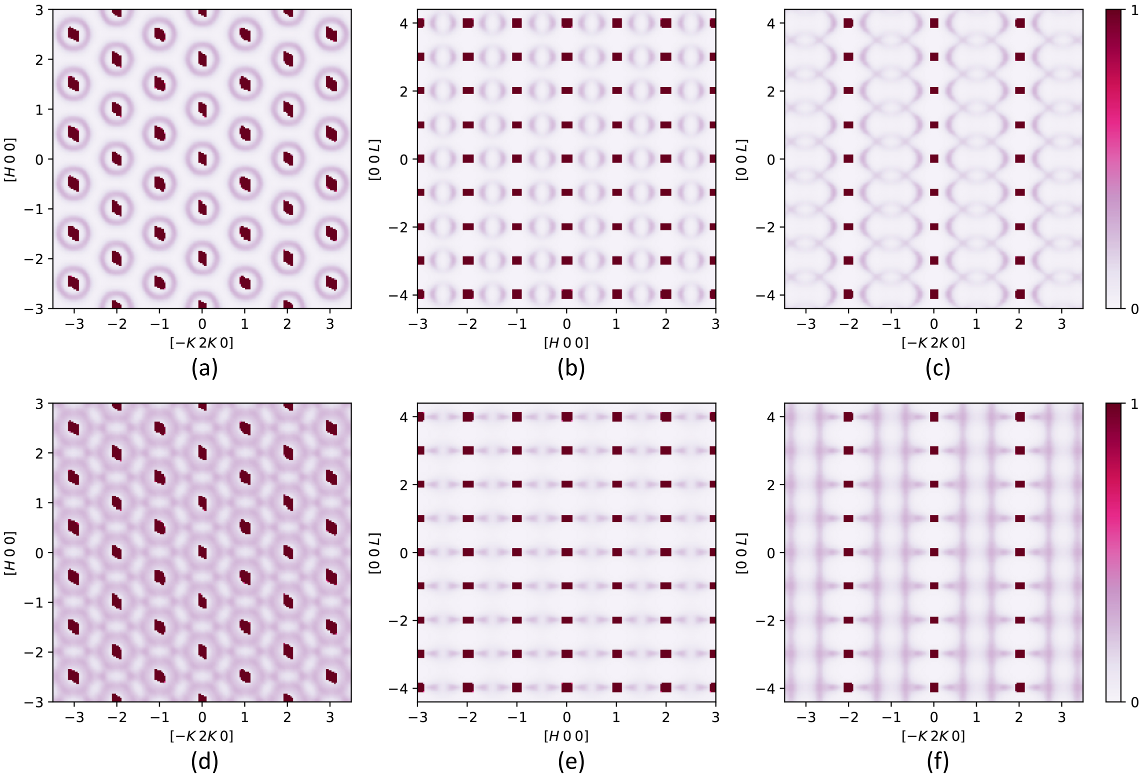

Figure 4.7. Simulated DPs of non-relaxed $V_{1+\delta}Sb$ using the local invariance model with **(a)**–**(c)** the trigonal bipyramidal clusters, and **(d)**–**(f)** the octahedral clusters in the [*H K* 0], [*H* 0 *L*] and [–*K* 2*K L*] planes, respectively.

sociated with coefficients J_{oh} and J_{tbp} to quantify the strength of each component.

MC simulations were carried out using a custom Python code. An ensemble of 20 configurations, each representing a 20 × 20 × 20 supercell of the unit cells containing a total of 16,000 sites, was used for each diffraction calculation. The configurations were initialised with a random distribution, whereby 40% of the sites were occupied. The MC steps again involved swap moves between nearest neighbours, following the Metropolis algorithm. The simulations were performed under quenching. The scattering patterns of the final configurations were computed using *Scatty* [53].

To explore the effect of a single cluster type, we ran the simulation setting either J to zero. The resulting DPs are presented in Figure 4.7. The images in the first row, which

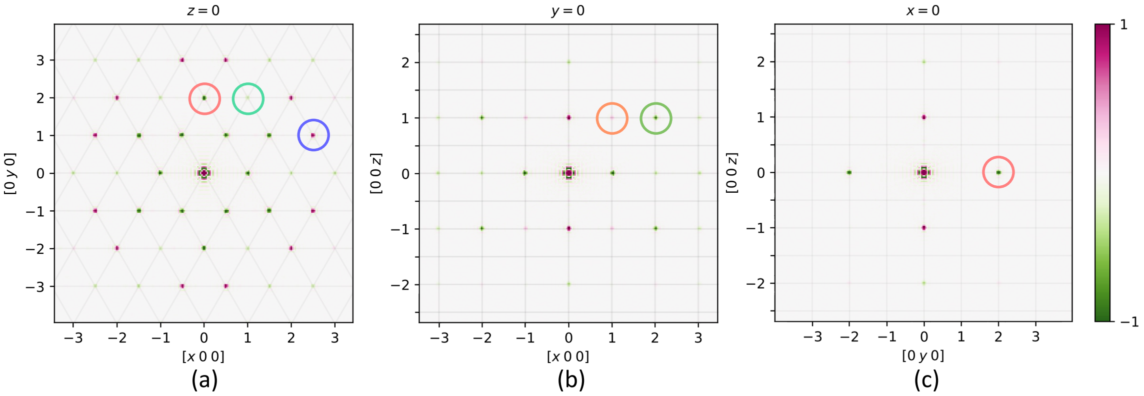

Figure 4.8. 3D-ΔPDF from the Brillouin zone-averaged diffraction data in the **(a)** [$x\,y$ 0], **(b)** [x 0 z], and **(c)** [0 $y\,z$] planes

represent the DPs calculated based on the vacancy distribution derived from the trigonal bipyramidal clusters, exhibit a closer resemblance to experiment. Given that these trigonal bipyramids correspond to the coordination of the V2/vacancy sites around the Sb atoms, it follows logically that the interaction between the Sb and V2 atoms necessitates local electroneutrality [56].

Although the local invariance model predicts geometric loci of allowed diffuse intensity, it is not mandatory for DS to be present at all points on these loci. The excessive flexibility granted by this model results in a number of degenerate states fulfilling the requirement. The Brillouin zone-averaged experimental DS in Figure 4.5 is the strongest at specific locations within the predicted region. Therefore, integration of additional pair interactions becomes necessary to simulate additional constraints that lead to the observed DPs.

4.2.3 Pair interaction model

To better understand the correlation in real space, the 3D-ΔPDF was calculated from the Brillouin zone-averaged diffraction data and presented in Figure 4.8. The resulting images have the impact of atomic displacement eliminated, leaving only features indicative of

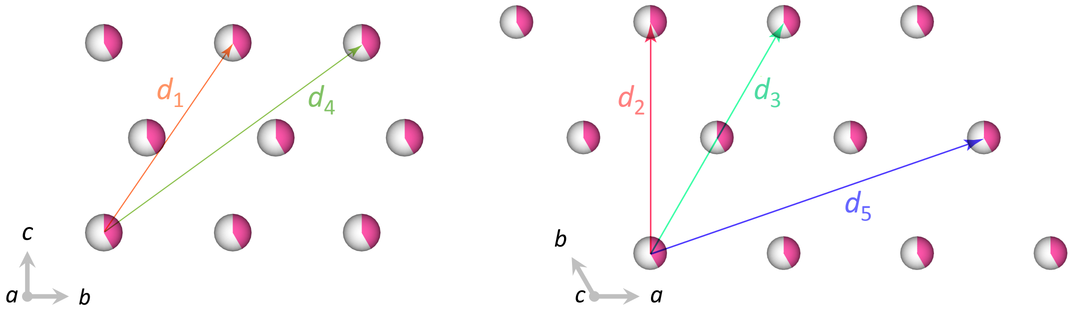

Figure 4.9. Diagram showing the disposition of the interaction vectors d_1 to d_5 used in the V2/vacancy ordering scheme. Symmetry-related vectors are omitted for clarity.

occupational disorder.

In the $[x\,y\,0]$ plane of the 3D-ΔPDF shown in Figure 4.8 (a), twelve intense positive peaks are observed at $[5/2, 1, 0]$ (circled in purple), and symmetry-related positions. This reveals a favourable correlation between V2 atoms found at distances over twice the length of the unit cell apart, as exemplified by the vector labelled d_5 in Figure 4.9. Through trial and error, it appeared that the inclusion of this interaction in the MC energy expression was essential. All attempts devoid of interactions of length d_5 failed to replicate the DS in the $[H\,K\,0]$ plane successfully.

Considering the significance of this relatively extended interaction vector, it inevitably follows that interactions between pairs separated by shorter vectors should also be considered. Hence, guided by the peak intensities observed in Figure 4.8, additional pairs with shorter distances were incorporated into the model. Five sets of neighbouring interactions were found relevant for the qualitative reproduction of the Brillouin zone-averaged DPs. Figure 4.9 presents one representative vector from each of these interaction vector sets. The numbers were assigned based on the lengths of the respective vectors, with d_1 being the shortest within the model. The corresponding 3D-ΔPDF signals are circled in the same colour in Figure 4.8 for easy identification. With this, the energy expression

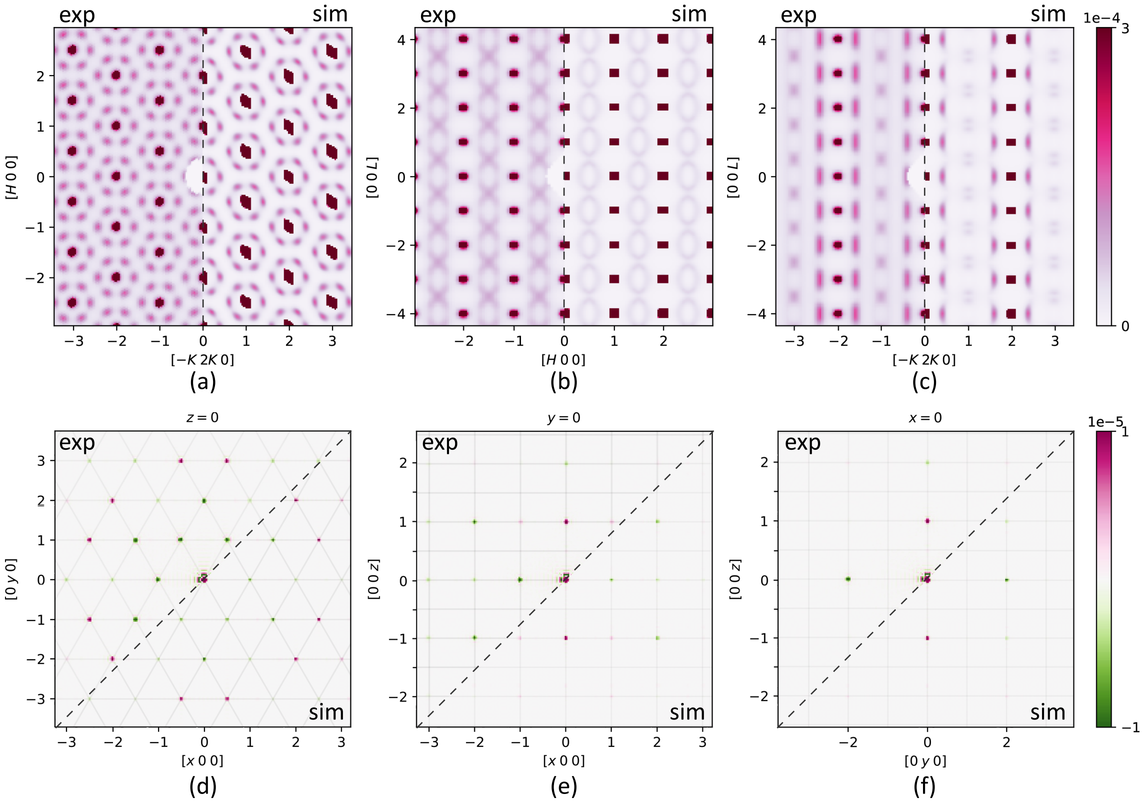

Figure 4.10. **(a)**–**(c)** Simulated non-relaxed DPs of $V_{1+\delta}Sb$ in the $[H\,K\,0]$, $[H\,0\,L]$ and $[-K\,2K\,L]$ planes, using the combined local invariance and pair interaction model (corresponding experimental DPs displayed on the left). **(d)**–**(f)** Calculated 3D-ΔPDF in the $[x\,y\,0]$, $[x\,0\,z]$, and $[0\,y\,z]$ planes based on the simulation (corresponding experimental images displayed on the top left).

can be written as

$$E = J_{\text{tbp}} \sum_{i=1}^{N_{\text{tbp}}} (s_i - s)^2 + \frac{1}{2} \sum_{k=1}^{5} J_k \cdot \sum_{|\mathbf{x}_i - \mathbf{x}_j| = d_k} \varepsilon_i \, \varepsilon_j \,, \tag{9}$$

where the first term represents the invariance sum of the trigonal bipyramidal clusters, and in the second term, we sum over all V2/vacancy pairs of sites i, j with distance equal to d_k, and $\varepsilon_i = \pm 1$ depending on whether the site i has (+1) or does not have (−1) a V atom. The coefficients $J_1, \ldots, J_5$ control the weights for pairs of each distance, where a negative value means that the corresponding separation is preferred, and a positive value means that the separation is penalised.

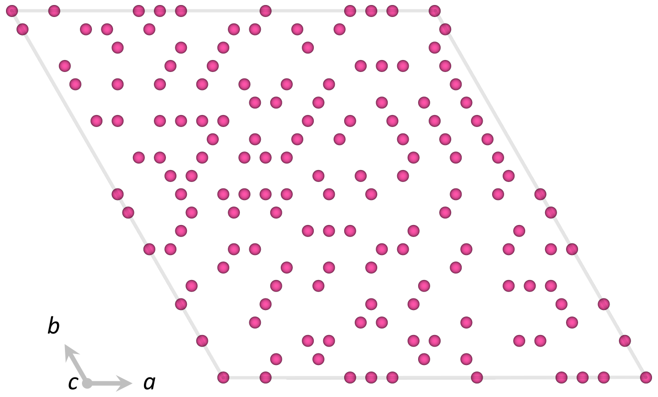

Figure 4.11. A representative layer of the final V2/vacancy distribution on a HCP lattice with 20 × 20 sites simulated based on the combined local invariance and pair interaction model. The size of the atoms is exaggerated.

MC simulations were carried out with the same protocol as described above, and a decent match was achieved when parameters J_1, J_3, J_5 were assigned negative values, and J_2 and J_4 were positive. The simulated DPs are shown on the right side of each image presented in the top row of Figure 4.10, with the corresponding measured DPs presented on the left for comparison. The 3D-ΔPDF derived from the simulated diffraction data is also compared with the experimental data at the bottom. A fairly satisfactory level of agreement was achieved between the observed and the simulated results, notably demonstrated in the close resemblance of the 3D-ΔPDF.

The J_{tbp} coefficient was set to a sufficiently large value, such that the local invariance term, on average, accounted for approximately 75% of the total energy reduction in the MC simulation. This term played a crucial role as it effectively allowed us to bypass the first three nearest-neighbour interactions, which are encompassed within the trigonal bipyramidal construction. Since this model served to approximate the ordering behaviour, the magnitudes of the J_k coefficients were set to be the same, with their signs being the only factor distinguishing whether the corresponding V2–V2 separation was favoured.

The alternating signs of the J_k coefficients, which successfully reproduced the diffraction data, might imply an attempt to uniformly distribute V2 within the HCP network, which appears to be constrained by the hexagonal symmetry. A representative layer depicting the final V2/vacancy distribution is shown in Figure 4.11. An additional configuration, inclusive of the Sb and V1 atoms, are provided in Appendix B.

While this model successfully generates physical structures with DPs closely resembling the observed ones, it is worth commenting that we are using *interactions* to capture *correlation*. In reality, these correlations could be the result of a synergy of shorter-range chemical interactions and geometric constraints.

4.3 Size effect in $V_{1+\delta}Sb$

Having established a model for the SRO in V2/vacancy distribution, our focus turned towards addressing the size effect. Based on the refined average structure in Section 4.1.1, it appears that Sb atoms exhibit the most pronounced vacancy-induced relaxation in planes perpendicular to the *c*-axis. Consequently, the investigation of the size effect started from correlations within this plane.

For closer examination, a magnified version of the $[x\,y\,0]$ layer of the 3D-ΔPDF is shown in Figure 4.12 (b). A prominent feature can be found around $[1/2, 1/3, 0]$ (labelled A), which is negative towards the centre and positive away from the centre. This signal, which represents the vector between Sb atoms and one of the three nearest V2/vacancy sites, implies that when a V2 atom is present at that site, the Sb atoms shift slightly away (corresponding vectors depicted by the pink arrows in (a)). This positive signal is slightly stretched since the Sb atoms can displace towards two different directions. Conversely,

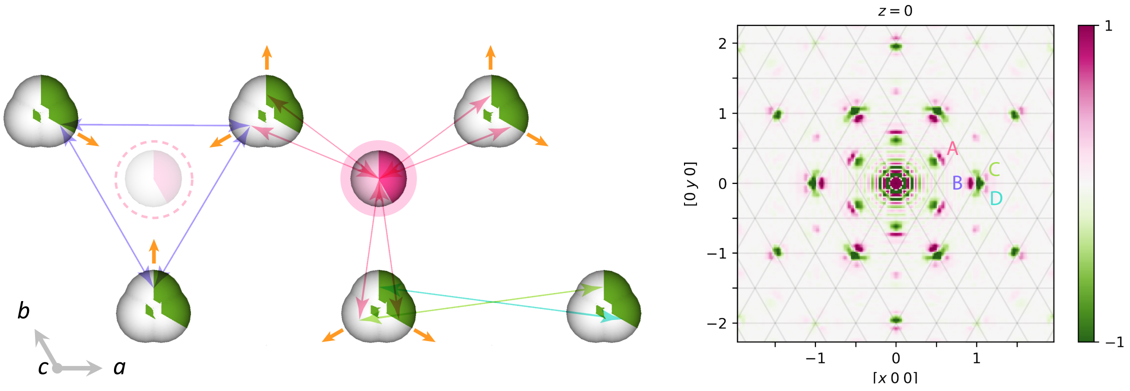

(a)

(b)

Figure 4.12. **(a)** Diagram showing the vacancy-induced displacement in the $z = 0.25$ layer of $V_{1+\delta}$Sb, with Sb in green and V in pink. **(b)** A magnified portion of the $[x\,y\,0]$ layer of the experimental 3D-ΔPDF.

the Sb atoms migrate towards the vacancy in the absence of V2. Within this plane, half of the six equivalent signals can be accounted for, which are related by 120° rotations. The remaining signals represent analogue in-plane correlations that are half the height of the unit cell above and below the presented plane.

At around $[1, 0, 0]$, another strong feature is observed, which represents the vectors between two nearest-neighbour Sb atoms or two nearest-neighbour V2 atoms. Given that an Sb ($Z = 51$) atom possesses more than double the electrons of a V ($Z = 23$) atom, this feature primarily indicates the interaction of the Sb–Sb pairs. A positive spot at position B signifies a higher probability to find Sb atoms closer together when they move towards a shared vacancy (depicted by the purple vectors in (a)). The fainter positive spots at positions C and D denote the probability of detecting Sb–Sb pairs at relative positions indicated by the green and blue vectors, as a consequence of the splitting.

As such, Sb splitting was integrated into the V2/vacancy distribution model. In cases when one of the three closest V2/vacancy sites around an Sb atom is vacant, the Sb atom shifts towards the vacancy. When two of these sites are vacant, the Sb atom moves

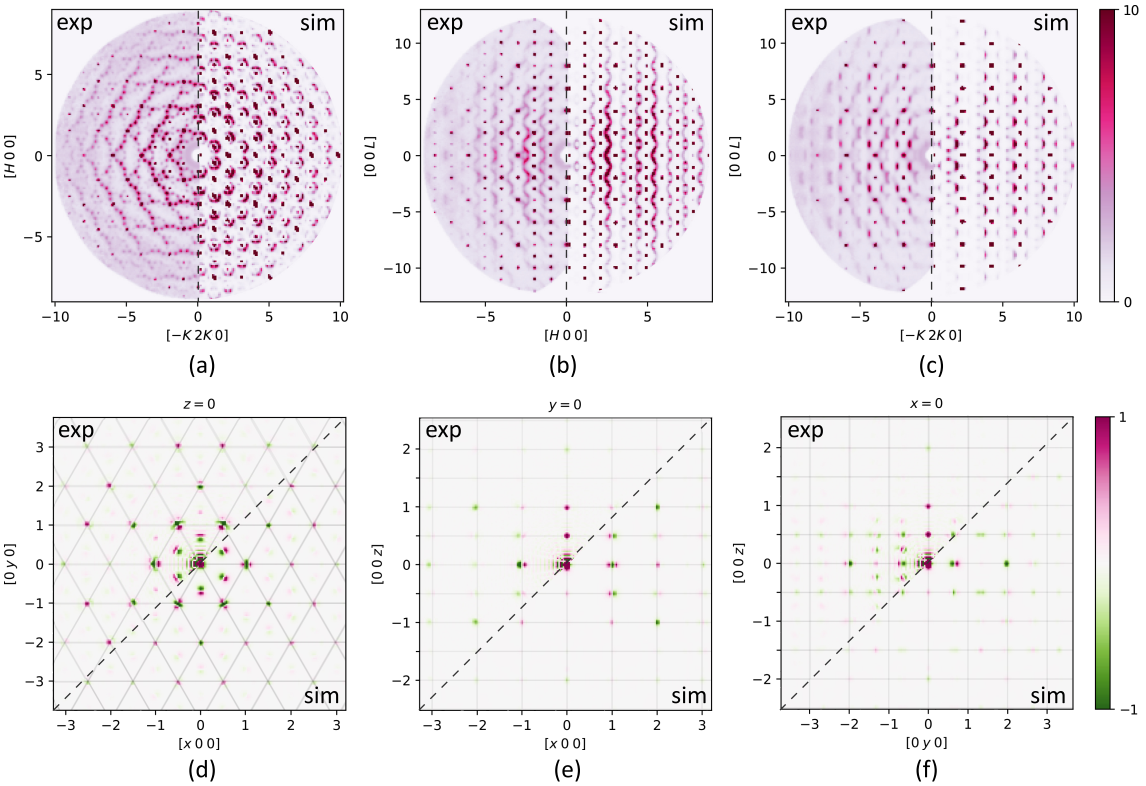

Figure 4.13. (a)–(c) Simulated X-ray DPs of the relaxed $V_{1+\delta}Sb$ in the [*H K* 0], [*H* 0 *L*] and [–*K* 2*K L*] planes (corresponding experimental DPs displayed on the left). **(d)–(f)** Calculated 3D-ΔPDF in the [*x y* 0], [*x* 0 *z*], and [0 *y z*] planes (corresponding experimental images displayed on the top left).

towards either of the vacant sites with equal probability. The magnitude of all displacements was set constant at 0.0405 Å — the value determined in our average structure refinement. In practice, the DPs obtained were not particularly sensitive to the magnitude of the displacement.

The simulated DPs and calculated 3D-ΔPDF based on the updated model are presented in Figure 4.13 as a comparison with the corresponding experimental results. The simulated DPs show considerable agreement, particularly within the [*H* 0 *L*] plane, where not only the shapes and positions, but also the relative intensity and the phase changes of the diffuse waves, are reproduced. The most pronounced discrepancy is seen in the [*H K* 0] plane, where the calculated DS only capture a subset of the observed features.

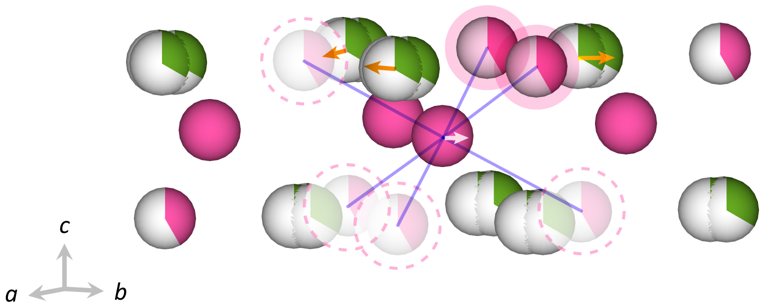

Figure 4.14. Diagram showing layers of the $V_{1+\delta}Sb$ structure from $z = 0.25$ to $z = 0.75$, with purple lines indicating the nearest-neighbour V2/vacancy sites of a V1 atom, and arrows showing the proposed direction of correlated displacement.

Despite this, the simulated 3D-ΔPDF in the $[x\,y\,0]$ plane exhibits satisfactory alignment with the experimental counterpart. We, therefore, suspect that correlations involving atoms across different layers may be responsible for the other diffuse features observed in the $[H\,K\,0]$ plane. In other words, although the induced displacement predominantly occurs within planes orthogonal to the *c*-axis, the atoms responsible for triggering this displacement are not confined within the same plane. This hypothesis is further supported in the $[0\,y\,z]$ layer in Figure 4.13 (f). While signals at $z = 0, \pm0.5$ align reasonably well, signals at $z = \pm0.25$ in the experimental data are entirely absent in the simulation.

4.3.1 Further improvements to the model

Based on the structure of $V_{1+\delta}Sb$, vectors with $z = 0.25$ represent the separation between the V2/Sb layers and the immediate next V1 layers. Therefore, we first considered incorporating the V1–V2 size effect into the model. This situation proved more complex than the Sb–V2 size effect, as each V1 atom is surrounded by six V2/vacancy sites both above and below, indicated by the purple lines in Figure 4.14. Depending on the number of occupied sites and their relative positions, there are likely many different scenarios of V1 displacements. This has potentially caused a broad electron density distribution around

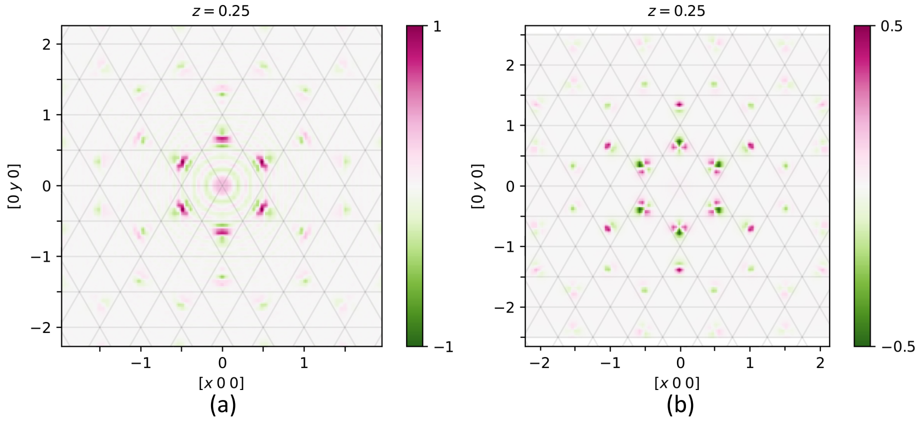

Figure 4.15. (**a**) Experimental [*x y* 0.25] cross-section of the 3D-ΔPDF of $V_{1+\delta}Sb$. (**b**) Simulated counterpart upon incorporating the V1–V2 size effect.

the V1 atoms, hindering the detection of its splitting in the average structure refinement.

Given that each V1 atom is typically surrounded by two or three V2 atoms in the model, we attempted to set up a simple simulation incorporating V1 relaxation only when the atoms are surrounded by two or three nearest-neighbour V2 atoms. Following a process of trial and error, we recognised a qualitative alignment in the DPs when the relaxation mode was as illustrated in Figure 4.14. This diagram describes a situation where the V2 atoms are present in sites circled in pink. Contrary to intuition, the V1 atom appears to move towards the occupied V2 sites, following the white arrow. One possible explanation could be the induced Sb displacements, indicated by the orange arrows, which trigger alterations in the local environment of the V1 atoms. This potentially forces the V1 atoms to move accordingly, given the greater size of the Sb atoms [71].

Figure 4.15 shows the experimental 3D-ΔPDF in the [*x y* 0.25] plane and the simulated image based on the model described above. The positive and negative signals appear approximately at comparable positions, but the match is not perfect. Furthermore, the simulated signals are half as intense as the observed signals. We, thus, draw two conclusions: first, the direction of V1 displacement broadly adheres to that proposed by the model; second, the stronger signals of the experimental data likely result from the involvement of the more electron-rich Sb atoms in the correlation.

Additionally, a DFT-based calculation was kindly performed by Thomas Nicholas using the Vienna Ab initio Simulation Package (VASP) [72], to probe the approximate behaviour of $V_{1+\delta}Sb$ under relaxation. Using the projector augmented wave (PAW) pseudopotential and the PBE/PBEsol exchange-correlation functionals, a fixed-cell geometric optimisation at 0 K was performed on MC simulated non-relaxed $4 \times 4 \times 4$ supercells. Preliminary results suggested that Sb atoms manifested the largest displacement from their average positions, which agrees with the previous results. Moreover, a moderate displacement was also observed in the V1 atoms. Consequently, future model development ought to focus on the displacement of V1 atoms, likely coupled to the displacement of Sb atoms.

4.4 Summary of model and relevance to TE properties

Using a combination of X-ray diffraction experiments, and Bragg and DS analysis, we investigated the structural disorder of $V_{1+\delta}Sb$ for the first time. The observed occupational disorder in the HCP V2/vacancy layers was rationalised using the combined local invariance and pair interaction model. The V2 atoms and vacancies display an almost alternating arrangement both within and between layers. Both the structure refinement and the simulations concur on a strong occupational-displacive coupling. The Sb atoms exhibit correlated displacement towards a nearest-neighbour vacancy. Additional evidence points towards a correlated relaxation of the V1 atoms, although a comprehensive model for this behaviour has yet to be established.

High-performance TE materials are characterised by high electrical conductivity, a large Seebeck coefficient, and low thermal conductivity. Conventionally, NiAs-type transition-metal pnictides are associated with high electrical conductivity [69]. The results summarised above lead to the postulation that the occupational disorder within the V2/vacancy network and the coupled displacive disorder of the Sb atoms could potentially induce effective phonon scattering, thereby reducing lattice thermal conductivity. However, an excessive disorder could negatively impact electron transport.

With regard to $V_{1+\delta}Sb$, the conduction band is possibly dominated by V, since it is an early transition metal possessing more valence electrons. As the V atoms exhibit less displacive disorder, the electron movement is possibly less hindered by the disorder. On the other hand, with a larger atomic mass and slower vibration, the Sb atoms are likely to contribute more to the low-energy phonons. Low-energy phonons, having a larger population and longer mean free paths, generally play a more crucial role in thermal transport. Hence, the more extensive Sb relaxation is likely to cause the scattering of low-energy phonons, which impedes thermal transport to a greater extent than electron transport.

Nevertheless, a more thorough investigation of the electronic and phononic band structures remains essential. An understanding of the TE performance of $V_{1+\delta}Sb$ eventually requires experimental measurements of the relevant physical parameters.

5

Conclusion

As diffuse scattering occurs in diverse forms across a broad spectrum of materials from many different physical or chemical origins, there has not been a unified, comprehensive method for its analysis [21]. The primary aim of this thesis, inspired by the local invariance rule, was to devise a universal local invariance MC energy scheme, for simulating the SRO in binary systems with occupational disorder. The subsequent investigation involved both theoretical simulations and applications to real materials.

One of the key findings from the 2D simulation is that insights into the local chemical constraints of the occupationally disordered binary system, particularly the predominant local cluster type, can be identified from the overall shape of the observed diffuse distribution. It has also been demonstrated, through an invented physical property termed boundary accessibility, that a change in the predominant cluster type can potentially influence certain physical properties. A potential application of this technique, therefore, involves investigations into how various synthetic methods or compositional tuning can induce changes in predominant cluster types, thereby allowing for the manipulation of material functionalities.

This integrated local invariance MC algorithm was applied to investigate the structural complexity of a potential TE material, $V_{1+\delta}Sb$. SC-XRD measurements revealed that this material has a $P6_3/mmc$ average space group with substantial correlated disorder. The 3D-ΔPDF analysis of the Brillouin zone-averaged and the original diffraction dataset indicated the presence of occupational disorder within the V2/vacancy HCP network, and the coupled displacive disorder of other atoms, respectively. Subsequent modelling generated configurations which reproduced the experimental results, and concluded on a constrained tendency towards a uniform distribution of V2 across the V2/vacancy network, and induced displacements of the Sb atoms towards the nearest-neighbour vacant sites. Meanwhile, potential correlations between the V1 and Sb displacements deserve further research. The structural analysis alone hints at the potential suitability of $V_{1+\delta}Sb$ as a TE material, likely due to the selective scattering of low-energy phonons. Nevertheless, experimental measurements of TE-related parameters have to be made, before any conclusions can be drawn.

During the process, 3D-ΔPDF proved extremely helpful in solving both the occupational disorder and the size effect modulation. More importantly, this investigation has shed light on several subtleties of our method. First, the local invariance model, although capable of sufficiently constraining the allowable diffuse intensity, is sometimes too flexible to induce a complete 3D ordering. Hence, additional constraints might be required on a case-by-case basis to produce specific versions of the structures which follow the local invariance rule. Nevertheless, this process can be greatly facilitated with the use of 3D-ΔPDF. Second, despite a successful qualitative reproduction of the DPs, it remains an interesting question how to interpret the relationship between the model and the underlying physics behind the structure.

Looking beyond this particular TE material, the extensive practice of tuning a wide range of physical properties via doping and substitution underscores the importance of understanding the resulting occupational disorder. The local invariance model, being completely generic for any disordered binary system, does not seek to provide a detailed picture of the local structure of the system under study. Instead, it serves as a convenient tool in modelling, to achieve local electroneutrality with fewer DoFs at play.

References

(1) Jaziri, N.; Boughamoura, A.; Müller, J.; Mezghani, B.; Tounsi, F.; Ismail, M. *Energy Rep.* **2020**, *6*, 264–287.

(2) Petsagkourakis, I.; Tybrandt, K.; Crispin, X.; Ohkubo, I.; Satoh, N.; Mori, T. *Sci. Technol. Adv. Mater.* **2018**, *19*, 836–862.

(3) Snyder, G. J.; Toberer, E. S. *Nat. Mater.* **2008**, *7*, 105–114.

(4) *Acta Crystallogr. A* **1992**, *48*, 922–946.

(5) Van Smaalen, S., *Incommensurate crystallography*; Oxford University Press: 2007.

(6) Keen, D. A.; Goodwin, A. L. *Nature* **2015**, *521*, 303–309.

(7) Wannier, G. H. *Phys. Rev.* **1950**, *79*, 357–364.

(8) Paddison, J. A. M.; Stewart, J. R.; Manuel, P.; Courtois, P.; McIntyre, G. J.; Rainford, B. D.; Goodwin, A. L. *Phys. Rev. Lett.* **2013**, *110*, 267207.

(9) Nakatsuji, S. et al. *Science* **2012**, *336*, 559–563.

(10) Trump, B. A.; Koohpayeh, S. M.; Livi, K. J. T.; Wen, J.-J.; Arpino, K. E.; Ramasse, Q. M.; Brydson, R.; Feygenson, M.; Takeda, H.; Takigawa, M.; Kimura, K.; Nakatsuji, S.; Broholm, C. L.; McQueen, T. M. *Nat. Comm.* **2018**, *9*, 2619.

(11) Welberry, T.; Withers, R.; Mayo, S. *J. Solid State Chem.* **1995**, *115*, 43–54.

(12) Matsuda, M.; Fujita, M.; Yamada, K.; Birgeneau, R. J.; Kastner, M. A.; Hiraka, H.; Endoh, Y.; Wakimoto, S.; Shirane, G. *Phys. Rev. B* **2000**, *62*, 9148–9154.

(13) Tan, G.; Zhao, L.-D.; Kanatzidis, M. G. *Chem. Rev.* **2016**, *116*, 12123–12149.

(14) Shakouri, A. *Annu. Rev. Mater. Res.* **2011**, *41*, 399–431.

(15) He, J.; Tritt, T. M. *Science* **2017**, *357*, 1369.

(16) Rowe, D. M., *CRC handbook of thermoelectrics*; CRC Press: 1995.

(17) Sales, B. C.; Mandrus, D.; Williams, R. K. *Science* **1996**, *272*, 1325–1328.

(18) Nolas, G. S.; Poon, J.; Kanatzidis, M. *MRS Bull.* **2006**, *31*, 199–205.

(19) Witting, I. T.; Chasapis, T. C.; Ricci, F.; Peters, M.; Heinz, N. A.; Hautier, G.; Snyder, G. J. *Adv. Electron. Mater.* **2019**, *5*, 1800904.

(20) Chen, C.; Xue, W.; Li, S.; Zhang, Z.; Li, X.; Wang, X.; Liu, Y.; Sui, J.; Liu, X.; Cao, F.; Ren, Z.; Chu, C.-W.; Wang, Y.; Zhang, Q. *Proc. Natl. Acad. Sci. USA* **2019**, *116*, 2831–2836.

(21) Welberry, T. R.; Goossens, D. J. *IUCrJ* **2014**, *1*, 550–562.

(22) Quarez, E.; Hsu, K.-F.; Pcionek, R.; Frangis, N.; Polychroniadis, E. K.; Kanatzidis, M. G. *J. Am. Chem. Soc.* **2005**, *127*, 9177–9190.

(23) Xia, K.; Nan, P.; Tan, S.; Wang, Y.; Ge, B.; Zhang, W.; Anand, S.; Zhao, X.; Snyder, G. J.; Zhu, T. *Energy Environ. Sci* **2019**, *12*, 1568–1574.

(24) Osborn, R. *Acta Crystallogr. B* **2023**, *79*, 99–100.

(25) Welberry, T. R.; Goossens, D. J.; Heerdegen, A. P.; Lee, P. L. *Z. Kristallogr. Cryst. Mater.* **2009**, *220*, 1052–1058.

(26) Jaeschke, E. J.; Khan, S.; Schneider, J. R.; Hastings, J. B., *Synchrotron light sources and free-electron lasers, Accelerator physics, instrumentation and science applications*; Springer Cham: 2016.

(27) Welberry, T. R.; Weber, T. *Crystallogr. Rev.* **2016**, *22*, 2–78.

(28) Cosier, J.; Glazer, A. M. *J. Appl. Crystallogr.* **1986**, *19*, 105–107.

(29) Giacovazzo, C. et al., *Fundamentals of Crystallography*, 3rd ed.; Oxford University Press: 2013.

(30) Schaub, P.; Weber, T.; Steurer, W. *Philos. Mag.* **2007**, *87*, 2781–2787.

(31) Sangiorgio, B.; Bozin, E. S.; Malliakas, C. D.; Fechner, M.; Simonov, A.; Kanatzidis, M. G.; Billinge, S. J. L.; Spaldin, N. A.; Weber, T. *Phys. Rev. Mater.* **2018**, *2*, 085402.

(32) Roth, N.; Beyer, J.; Fischer, K. F. F.; Xia, K.; Zhub, T.; Iversena, B. B. *IUCrJ* **2021**, *8*, 695–702.

(33) Chan, E. J. *J. Appl. Crystallogr.* **2015**, *48*, 1420–1428.

(34) Welberry, T. R.; Goossens, D. J. *Acta Crystallogr. A* **2007**, *64*, 23–32.

(35) Metropolis, N.; Rosenbluth, A. W.; Rosenbluth, M. N.; Teller, A. H.; Teller, E. *J. Chem. Phys.* **1953**, *21*, 1087–1092.

(36) Butler, B. D.; Welberry, T. R. *J. Appl. Crystallogr.* **1994**, *27*, 742–754.

(37) Welberry, T. R.; Christy, A. G. *Phys. Chem. Miner.* **1997**, *24*, 24–38.

(38) Pasciak, M.; Welberry, R. *Z. Kristallogr.* **2010**, *226*, 113–125.

(39) Hasnip, P. J.; Refson, K.; Probert, M. I. J.; Yates, J. R.; Clark, S. J.; Pickard, C. J. *Phil. Trans. R. Soc. A* **2014**, *372*, 20130270.

(40) Xue, H.-T.; Yu, X.-D.; Aarons, J.; Tang, F.-L.; Lu, X.-F.; Rena, J.-Q. *Phys. Chem. Chem. Phys.* **2020**, *22*, 14694–14703.

(41) Welberry, T. R., *Diffuse X-Ray Scattering and Models of Disorder*; Oxford University Press: 2022.

(42) *CrysAlisPRO*, Oxford Diffraction/Agilent Technologies UK Ltd, Yarnton, England.

(43) Petříček, V.; Dušek, M.; Palatinus, L. *Z. Kristallogr.* **2004**, *229*, 345–352.

(44) Simonov, A. *Meerkat*, Version 0.3.7, A program for reciprocal space reconstruction, 2020.

(45) Proffen, T.; Page, K. L.; McLain, S. E.; Clausen, B.; Darling, T. W.; TenCate, J. A.; Lee, S.-Y.; Ustundag, E. *Z. Kristallogr. Cryst. Mater.* **2005**, *220*, 1002–1008.

(46) Weber, T.; Simonov, A. *Z. Kristallogr.* **2012**, *227*, 238–247.

(47) Simonov, A.; Baerdemaeker, T. D.; Boström, H. L. B.; Gómez, M. L. R.; Gray, H. J.; Chernyshov, D.; Bosak, A.; Bürgi, H.-B.; Goodwin, A. L. *Nature* **2019**, *578*, 256–260.

(48) Krogstad, M. J.; Rosenkranz, S.; Wozniak, J. M.; Jennings, G.; Ruff, J. P. C.; Vaughey, J. T.; Osborn, R. *Nat. Mater.* **2020**, *19*, 63–68.

(49) Kobas, M.; Weber, T.; Steurer, W. *Phys. Rev. B* **2005**, *71*, 224205.

(50) Goossens, D. J. *Metals* **2016**, *6*, 33.

(51) Kirkpatrick, S.; Gelatt, C. D.; Vecchi, M. P. *Science* **1983**, *220*, 671–680.

(52) Roth, N.; Zhu, T.; Iversen, B. B. *IUCrJ* **2020**, *7*, 673–680.

(53) Paddison, J. A. M. *Acta Crystallogr. A* **2019**, *75*, 14–24.

(54) Sanchez, J. M.; Ducastelle, F.; Gratias, D. *Phys. A: Stat. Mech. Appl.* **1984**, *128*, 334–350.

(55) Withers, R. L. *Z. Kristallogr.* **2005**, *220*, 1027–1034.

(56) Pauling, L., *The nature of the chemical bond and the structure of molecules and crystals: An introduction to modern structural chemistry*, 3rd ed.; Cornell University Press: 1960.

(57) Sauvage, M.; Parthé, E. *Acta Crystallogr. A* **1972**, *28*, 607–616.

(58) Billingham, J.; Bell, P. S.; Lewis, M. H. *Acta Crystallogr. A* **1977**, *32*, 216–224.

(59) De Ridder, R.; van Tendeloo, G.; van Dyck, G.; Amelinckx, S. *J. Phys. Colloq.* **1977**, *38*, 178–186.

(60) Withers, R.; Welberry, T.; Brink, F.; Norén, L. *J. Solid State Chem.* **2003**, *170*, 211–220.

(61) Rao, Y.; Curtin, W. A. *Acta Mater.* **2022**, *226*, 117621.

(62) Billingham, J.; Bell, P. S.; Lewis, M. H. *Acta Crystallogr. A* **1972**, *28*, 602–606.

(63) Schwarz, H. A., *Bestimmung einer speciellen Minimalfläche*; Dümmler: 1871.

(64) Welberry, T. R.; Butler, B. D. *J. Appl. Crystallogr.* **1994**, *27*, 205–231.

(65) Li, Y.; Smith, N. P.; Rexhausen, W.; Schofield, M. A.; Guptasarma, P. *J. Phys. Mater.* **2020**, *3*, 015008.

(66) Cardarelli, F., *Materials Handbook: A Concise Desktop Reference*; Springer Science & Business Media: 2008.

(67) Grison, B.; Beck, P. A. *Acta Crystallogr.* **1962**, *15*, 807–808.

(68) Schubert, K.; Meissner, K. G.; Raman, A.; Rossteutscher, W. *Sci. Nat.* **1964**, *51*, 287.

(69) Schubert, K.; Meissner, K. G.; Raman, A.; Rossteutscher, W. *J. Solid State Chem.* **1973**, *7*, 255–261.

(70) Schmidt, E.; B Neder, R. *Acta Crystallogr. A* **2017**, *73*, 231–237.

(71) Slater, J. C. *J. Chem. Phys.* **1964**, *41*, 3199–3204.

(72) Kresse, G.; Furthmüller, J. *Phys. Rev. B* **1996**, *54*, 11169–11186.

A

Allowed loci for diffuse intensity

This appendix lists the equations for the allowed geometric loci for diffuse intensity in reciprocal space for the 2D local invariance model. The graphical representations of the equations were shown in the bottom rows of Figures 3.1 and 3.2. These loci were calculated based on Equation (4), by explicitly substituting in the coordinates of atoms in the corresponding local clusters.

Figure 3.1 (g)

$$\cos[\pi(h+k)] + \cos[\pi(h-k)] = 0$$

Figure 3.1 (h)

$$\cos(2\pi h) + \cos(2\pi k) = 0$$

Figure 3.1 (i)

$$\cos(2\pi h) + \cos(2\pi k) + \cos[2\pi(h+k)] = 0$$

$$\cos(2\pi h) + \cos(2\pi k) + \cos[2\pi(h-k)] = 0$$

Figure 3.2 (g)

$$\exp\left[\mathrm{i}\pi\left(h+\frac{\sqrt{3}}{2}k\right)\right]+\exp\left[\mathrm{i}\pi\left(-h+\frac{\sqrt{3}}{2}k\right)\right]+\exp\left[\mathrm{i}\pi\left(-\frac{\sqrt{3}}{2}k\right)\right]=0$$

$$\exp\left[\mathrm{i}\pi\left(h-\frac{\sqrt{3}}{2}k\right)\right]+\exp\left[\mathrm{i}\pi\left(-h-\frac{\sqrt{3}}{2}k\right)\right]+\exp\left[\mathrm{i}\pi\left(\frac{\sqrt{3}}{2}k\right)\right]=0$$

Figure 3.2 (h)

$$\cos(\pi h)+\cos(\sqrt{3}\pi k)=0$$

$$\cos\left[\pi\left(\frac{3}{2}h+\frac{\sqrt{3}}{2}k\right)\right]+\cos\left[\pi\left(-\frac{1}{2}h+\frac{\sqrt{3}}{2}k\right)\right]=0$$

$$\cos\left[\pi\left(-\frac{3}{2}h+\frac{\sqrt{3}}{2}k\right)\right]+\cos\left[\pi\left(\frac{1}{2}h+\frac{\sqrt{3}}{2}k\right)\right]=0$$

Figure 3.2 (i)

$$\cos(2\pi h)+\cos[\pi(h+\sqrt{3}k)]+\cos[\pi(h-\sqrt{3}k)]=0$$

B

Configuration of non-relaxed $V_{1+\delta}Sb$

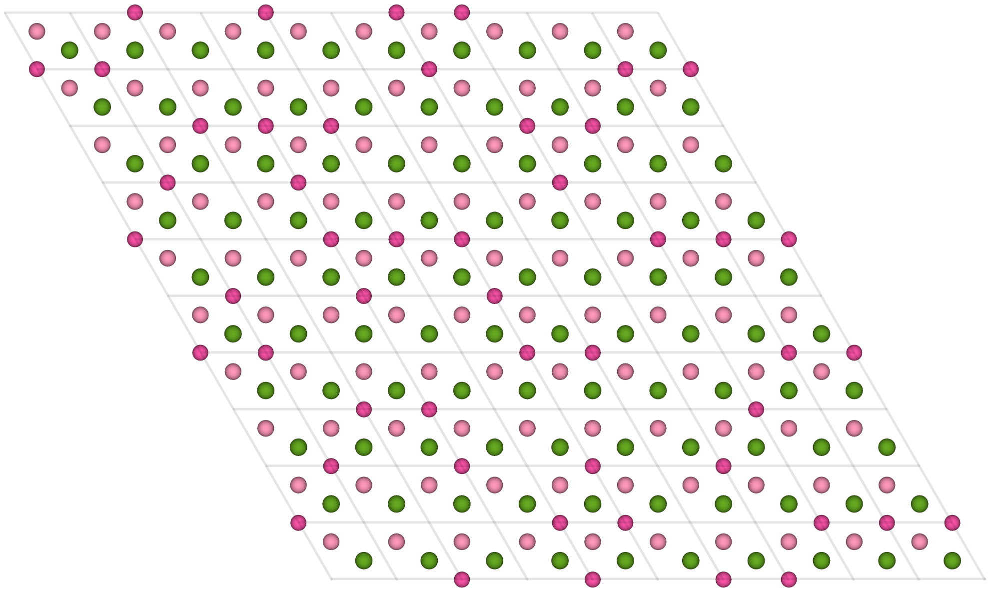

Figure B.1. Half-unit cell thick slice of a representative portion of the final non-relaxed atom distribution in a 10 × 10 supercell, projected along the *c* axis. This was calculated from the combined model detailed in Section 4.2.3. The Sb, V1 and V2 atoms are featured in green, light pink, and dark pink respectively. The unit cell origin has been shifted to a V2 atom as opposed to a V1 atom in the unit cell presented in Figure 4.1.